2005

Nondestructive Evaluation Of Thermal Barrier Coatings With Thermal Wave Imaging And Photostimulated Luminescence Spectroscopy

Barbara Franke
University of Central Florida

NON-DESTRUCTIVE EVALUATION OF THERMAL BARRIER COATINGS WITH THERMAL WAVE IMAGING AND PHOTOSTIMULATED LUMINESCENCE SPECTROSCOPY

by

BARBARA FRANKE
B.S. University of Central Florida, 2004

A thesis submitted in partial fulfillment of the requirements
for the degree of Master of Science
in the Department of Mechanical, Materials, and Aerospace Engineering
in the College of Engineering and Computer Science
at the University of Central Florida
Orlando, Florida

Summer Term
2005

ABSTRACT

Gas Turbine manufacturers strive for increased operating temperatures of gas turbine engines to improve efficiency and performance. One method of increasing the temperature beyond material limits is by applying thermal barrier coatings (TBCs) to hot section components. TBCs provide a thermal gradient between the hot gases and metallic substrate, and allow an increase in turbine inlet temperatures of 100-150°C. However, spallation of TBCs can cause catastrophic failure of turbine engines by incipient melting of the substrate. To prevent such an occurrence, non-destructive evaluation (NDE) techniques are critical for quality control, health monitoring, and life assessment of TBCs. Two techniques in development for this purpose are thermal wave imaging (TWI) and photostimulated luminescence (PL) spectroscopy.

TWI is a promising NDE technique with the ability to detect integrity and thickness of TBCs. In this study, TWI was employed as an NDE technique to examine as-coated TBCs with varying thicknesses, and thermally-cycled TBCs for initiation and progression of subcritical-subsurface damage as a function of thermal cycling. TWI and thermal response amplitude were correlated to the microstructural characteristics and damage progression of TBCs based on phenomenological expressions of thermal diffusion. The TBC specimens examined consisted of air plasma sprayed ZrO_2 - 7wt.% Y_2O_3 on NiCoCrAlY bond coats with Haynes 230 superalloy substrate. As-coated specimens of varying thicknesses were evaluated by TWI to examine its applicability as a thickness measurement tool. It was found that heat dissipation through the TBC following pulsed excitation by xenon flash lamps initially followed the 1-D law of conduction and deviated from it as a function of thickness and time. The deviation resulted from quick dissipation of heat into the conductive metallic substrate. Therefore, with calibration, TWI can be

used as a tool for YSZ thickness measurements of APS TBCs in the as-coated condition for quality control measures.

Specimens of uniform thickness were evaluated as a function of thermal cyclic oxidation for subcritical-subsurface damage detection. Thermal cycling was carried out in air with 30-minute heat-up, 10-hour dwell at 1150°C, 30-minute air-quench and 1-hour hold at room temperature. During thermal cycling, TBC specimens were evaluated non-destructively by TWI at room temperature every 10 to 20 thermal cycles, and selected specimens were removed from thermal cycling for microstructural analysis by scanning electron microscopy (SEM). Higher thermal response amplitude associated with disrupted heat transfer was observed where localized spallation at or near the YSZ/TGO interface occurred. The health of the TBC was monitored by a rise in thermal response amplitude which may indicate a coalescence of microcracks to a detectable level.

PL has been developed to measure stress, and detect subsurface damage and polymorphic transformation within the thermally grown oxide (TGO) of TBCs. PL was employed in this study as an NDE technique for TBCs to correlate subsurface damage as a function of thermal cyclic oxidation. The TBCs consisted of ZrO_2 – 7 wt.% Y_2O_3 applied by electron beam physical vapor deposition with an as-coated (Ni,Pt)Al bond coat on a CMSX-4 superalloy substrate. Specimens were thermally cycled with a 10 minute ramp to a peak temperature of 1121°C, 40 minute hold at peak temperature, and 10 minute forced air quench. The TBCs were periodically removed from thermal cycling for NDE using PL until failure. Two specimens were removed from thermal oxidation after 10% and 70% of the average lifetime for microstructural analysis by SEM. During initial thermal cycling, metastable phases and polymorphic transformations of the Al_2O_3 scale were examined by PL. The polymorphic transformation from a metastable phase to

equilibrium α-Al_2O_3 was detected. Since metastable phases are thought to be detrimental to coating lifetime, detection of these phases by PL can be used as a quality control tool.

Nearing end-of-life, relief of the TGO from the compressive residual stress arising from thermal expansion mismatch was detected with PL and confirmed with microstructural analysis that revealed damage initiation (e.g. microcracking within the TGO scale parallel to the interfaces.) Rise in luminescence near the R-line frequency for polycrystalline α-Al_2O_3 without any residual stress (i.e. ν = 14402 cm^{-1} and ν = 14432 cm^{-1}) corresponded to regions where cracked TGO was adhered to YSZ and not exposed to compressive stresses from thermal expansion mismatch upon cooling.

This manuscript was written in memory of my sister, Christine Franke.
I dedicate this work to my family.

ACKNOWLEDGMENTS

I would like to express my gratitude towards my advisor, Dr. Yong-ho Sohn, who has opened many doors of opportunity for me. His technical guidance, patience, and consideration are deeply appreciated and will not be forgotten.

I would like to give special thanks my committee members Dr. Vimal Desai, Dr. Kevin Coffey, Dr. Helge Heinrich, and Mr. Jeff Price.

This work was made possible though the financial support of Solar Turbines Incorporated and the University Turbine Systems Research (UTSR) program of National Energy Technology Laboratry (NETL), US-DOE. I would like to acknowledge my appreciation for the industrial fellowship program sponsored by UTSR, in which I was awarded two internships with Solar Turbines Incorporated. I would also like to specifically thank Jeff Price, Xiaoqun Chen, and Zaher Mutasim with Solar Turbines Incorporated for technical guidance.

The love and support from my family and friends throughout my education is sincerely cherished.

I am grateful for my fellow lab members who have helped me along the way: Dr. Jai-Won Byeon, Narayana Garimella, Balaji Jayaraj, Sankar Laxman, Jing Liu, Mu Nan, Rashmi Mohanty, David Miranda, Travis Patterson, Emmanuel Perez, Abby Elliot Puccio, and Srinivas Vishweswaraiah, and also to the new additions Monica Hopkins and Nathan Hotaling.

A very special thanks goes to Mr. Balaji Jayaraj who has given me so much technical support throughout my research and guidance in the science and in life.

And to Emmanuel Perez who tolerates me as much as I tolerate him. Thanks for being a good friend.

TABLE OF CONTENTS

LIST OF FIGURES

LIST OF TABLES

LIST OF ACRONYMS/ABBREVIATIONS

APS	Air Plasma Spray
CCD	Charged Coupled Device
COZ	Continuous Oxide Zone
CVD	Chemical Vapor Deposition
EB-PVD	Electro-Beam Physical Vapor Deposition
c	Cubic Flourite Phase of Zirconia
FCC	Face-Centered-Cubic
LPPS	Low Pressure Plasma Spray
m	Monoclinic Phase of Zirconia
MOZ	Mixed Oxide Zone
NDE	Non-destructive Evaluation
PL	Photostimulated Luminescence
PS	Plasma Spray
PT	Pulsed Thermography
SEM	Scanning Electron Microscopy
t	Tetragonal Phase of Zirconia
t’	Non-transformable Tetragonal Phase of Zirconia
TBC	Thermal Barrier Coating
TGO	Thermally Grown Oxide
TRIT	Turbine-Rotor-Inlet-Temperature
TWI	Thermal Wave Imaging
XEDS	X-Ray Energy Dispersive Spectroscopy
YSZ	Yttria Stabilized Zirconia

1. INTRODUCTION

The efficiency and performance of gas powered turbine engines for power generation or aero applications depend greatly on the turbine-rotor-inlet-temperature (TRIT).[1] The need for gas turbine manufacturers to increase operating temperatures has driven the development of materials and processes for demanding high temperature application. A major material development for high temperatures was the advent of superalloys, shortly before the Second World War. The introduction of gas turbine engines created higher demands for such alloys and the improvement of materials and processes.[2]

Nickel-based superalloys typically comprise of 10-20 at.% Cr, up to 8 at.% Al and Ti, 5-10 at.% Co, small amounts of B, Zr, and C, and may also contain Mo, W, Ta, Hf, and Nb. The two major phases present in these alloys are γ and γ'. The γ-phase is a continuous matrix of face-centered-cubic (FCC) nickel-based austenite, commonly with high percentages of solid solution elements such as Co, Cr, Mo, and W. The γ' phase has an ordered $L1_2$ crystal structure based on the FCC lattice. This phase is primarily the strengthening phase through coherent precipitation of $Ni_3(Al,Ti)$.[3]

Ni-based superalloys are designed to withstand load-bearing applications at temperatures up to 90% of their melting temperatures. TBCs were developed to raise the TRIT higher than the superalloy could withstand. The thin ceramic layer provides insulation to the superalloy while raising the temperature 200-300°F higher than the incipient melting point of the superalloy. [4] TBC, a multilayer coating system, has an insulating ceramic topcoat that provides a thermal gradient between the hot gases and the metallic substrate. [4,5,6] This ceramic topcoat, in general, consists of 7-8 wt.% yttria stabilized zirconia (YSZ) with high thermal expansion coefficient and low thermal conductivity.[5,4,6] The YSZ topcoats are applied by either air plasma spray (APS) or

electron beam physical vapor deposition (EB-PVD). Underneath the YSZ is a metallic bond coat of either MCrAlY (M = Ni and/or Co) or (Ni,Pt)Al. The bond coat protects the superalloy substrate from oxidation by serving as an aluminum source for the formation of a thermally grown oxide (TGO), generally consisting of α-Al_2O_3 that forms between the bond coat and topcoat. The TGO is a critical part of the coating system because it is at or near this interface that spallation failure of TBCs occurs.[7,8] Since TBCs allow operating temperatures that exceed the substrate limitations, spallation may lead to catastrophic failure. NDE techniques are therefore critical for life assessment and health monitoring of TBCs to prevent such an occurrence. In this study, two NDE techniques were evaluated as damage detection tools for TBCs by correlating microstructural failure mechanisms with NDE analyses.

Two NDE techniques were investigated in this study: thermal wave imaging (TWI) and photostimulated luminescence (PL) spectroscopy. TWI provides a non-intrusive means of detecting subsurface damage in TBCs.[9,10,11,12] In this investigation, TWI was employed for evaluation of APS TBCs with NiCoCrAlY bond coats for quality control and health monitoring. As-coated TBCs were examined by TWI as a function of YSZ thickness. Also, TWI was employed as a function of thermal cyclic oxidation to detect subcritical, subsurface damage initiation and progression. Thermal images and thermal response amplitude obtained by TWI were correlated to the microstructural development observed by scanning electron microscopy (SEM) with an emphasis on detecting damage initiation and progression.

With PL, signal from underneath the ceramic topcoat can provide information to attain residual stress and phase constituents within the TGO. This study utilized EB-PVD TBCs with an as-coated (Ni,Pt)Al bond coat on a CMSX-4 superalloy substrate. PL as a function of thermal

cycling was examined to detect subsurface damage and metastable phases. Luminescence was linked to the microstructural features of subsurface damage by SEM.

2. LITERATURE REVIEW

2.1. Thermal Barrier Coatings

Thermal barrier coatings (TBCs) depicted in Figure 1 are applied to hot section components of advanced gas turbine engines to provide a thermal gradient between the hot combustion gases and metallic substrate. Components with TBCs are internally cooled turbine blades and vanes, combustor liners, and nozzles. TBCs allow reduced cooling air requirements through internal passages while maintaining the turbine durability, thereby increasing overall turbine efficiency and reducing emissions. Processing of the coatings can sometimes produce uncertainty in reliability and, consequently, advantages of the application of TBCs are not always utilized in engine design. It is therefore necessary to understand each component of the coating system, the failure mechanisms, and the function and applicability of non-destructive evaluation (NDE) techniques that can monitor the quality and health of the coatings. The following sections will explore the composition, processing, and microstructure of the ceramic topcoat, the metallic bond coat, failure mechanisms of TBC systems, and NDE techniques for quality control and health monitoring of TBCs.

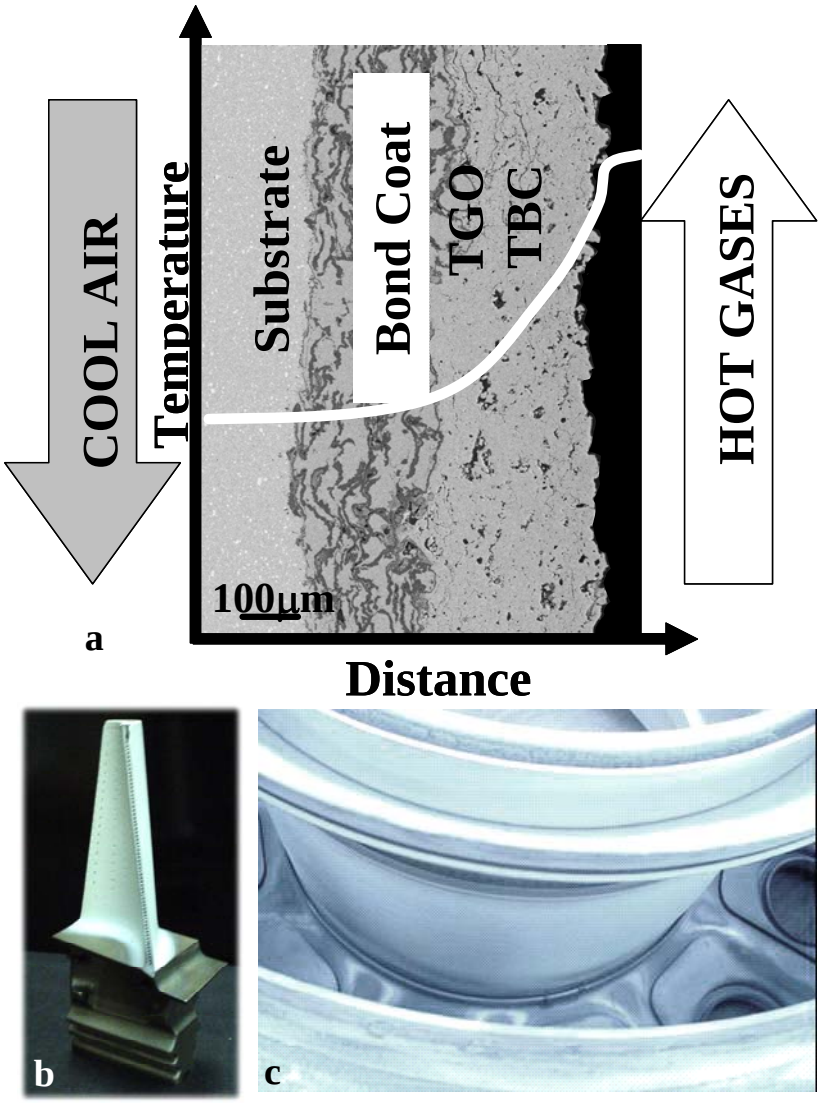

Figure 1. (a) Backscatter electron image of an air plasma sprayed thermal barrier coating superimposed with the temperature gradient across the ceramic topcoat. TBCs are applied to turbine components such as cooled (b) turbine blades and vanes and (c) combustor liners.

2.1.1. Ceramic Topcoat

The material choice suitable for the ceramic topcoat layer should entail as many of the following properties as possible: high melting point; low density; high surface emissivity; high thermal shock resistance; low vapor pressure; resistance to oxidation or chemical environment; low thermal conductivity; high coefficient of thermal expansion; and resistance to gaseous and

particulate erosion. The base material for TBCs is zirconia (ZrO_2) since many properties are well suited for TBC application, such as low thermal conductivity, high coefficient of thermal expansion, and excellent thermal shock resistance.[4,13] ZrO_2 exists in three crystallographic phases at low, intermediate, and high temperatures: monoclinic (m), tetragonal (t), and cubic (c), respectively, depicted in the phase diagram of ZrO in Figure 2.[14] Upon heating, pure zirconia undergoes phase transformations from monoclinic to tetragonal at about 1180°C (1450 K), and from tetragonal to cubic at about 2370°C (2640 K). The martensitic phase transformation from monoclinic to tetragonal causes a detrimental volume contraction of 3% - 12%, which causes a loss of physical integrity and may cause the ceramic to crack and crumble. To avoid the unfavorable phase transformation, the zirconia must be stabilized at room temperature in the tetragonal or cubic form.

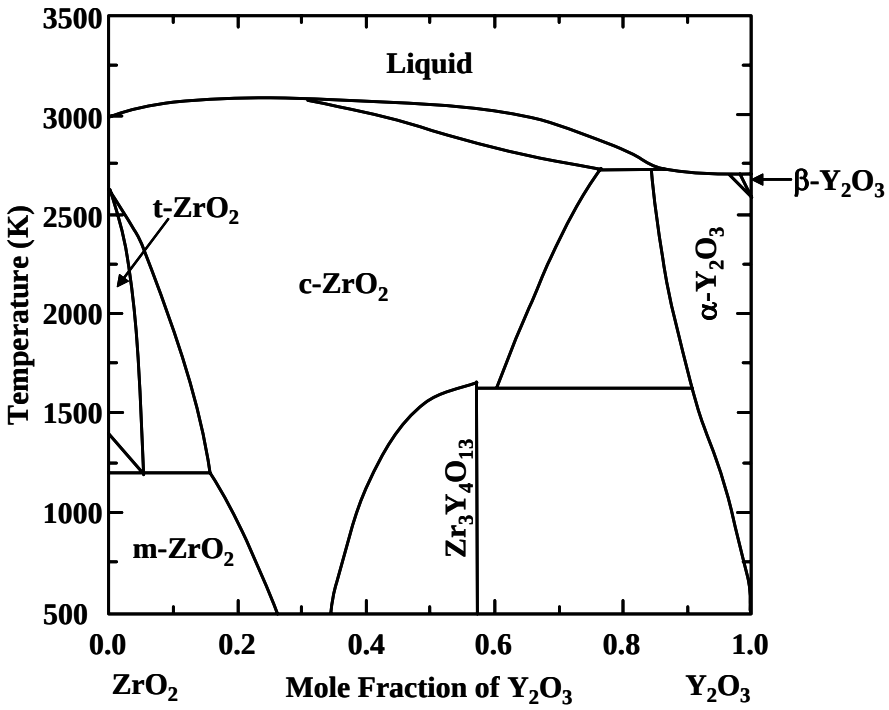

Figure 2. The ZrO_2-Y_2O_3 phase diagram.

Several oxides have been used to stabilize zirconia, but the most beneficial effects result from the addition of 6-8 wt.% yttria, giving the most stable solid solutions. There are many factors that influence the behavior of stabilization, yet the mechanism responsible for it is not certain. Such influential factors include annealing temperature, duration at peak temperature, quench rates, and grain size. Stabilized zirconia can be produced by adding 2-3 mol% Y_2O_3 to zirconia and sintering at 1400 – 1600°C. When appropriately cooled to room temperature, a tetragonal phase is present, and may contain small amounts of cubic phase or contain a cubic phase matrix depending on the precise Y_2O_3 content and preparation conditions. This polycrystal yttria-tetragonal zirconia phase produces an extremely strong ceramic with high strength and fracture toughness. The fracture toughness is thought to be a result of transformation toughening, wherein high stress drives a phase transformation to the monoclinic phase to dissipate the energy. This phase, though, has drawbacks, including possible loss of strength if exposed to low temperature water vapor, a return to monoclinic-tetragonal phase behavior, and a requirement of grain size to be less than 1μm.

A more appropriate phase for TBCs is the partially stabilized tetragonal (t') phase, which is not transformable. This phase is produced by heating 4-5 mol% Y_2O_3 with ZrO_2 to the cubic phase region in excess of 2200°C and quenched rapidly. Although the t' phase is not as strong as the t phase, t' exceeds t in resistance to high-temperature thermal decomposition and to degradation by H_2O vapor. The most successful stabilized zirconia TBCs contain about 8wt.% Y_2O_3. Processing and application of the ceramic also influences the properties of the coating. There are two principle processes of applying YSZ: plasma spray (PS) and electron beam

physical vapor deposition (EB-PVD), both of which could induce rapid quenching. Each of these processes will be discussed in detail.

2.1.1.1. Plasma Spray

PS TBCs have been commercially implemented in gas turbine engines since the mid-1980s. Great benefits of this process are the ability to produce durable and reproducible coatings at low cost. PS combines particle melting, rapid solidification, and consolidation in a single process.[15] The plasma spray torch is shown schematically in Figure 3, where the cathode is made from tungsten and the anode from water cooled copper. A carrier gas, typically argon, yet sometimes with additions of diatomic gases such as hydrogen, helium, or nitrogen, flows between the electrodes, is ionized by creating an electric arc between the electrodes, and a high-pressure-gas plasma is formed. The gas temperature (as a result of the arc) may exceed 30,000°C. In turn, the gas expands in volume leading to increased pressure and velocity as it exits the nozzle. At or near the nozzle exit, solid powders are fed into the gas stream, where they are heated and accelerated by the high-temperature, high-velocity plasma. The powders become molten and are accelerated to velocities on the order of 100 – 550 m/s. The molten droplets collide with the substrate (typically with a rough surface), flatten, and cool, adhering to the coarse surface by interlocking with surface irregularities. Therefore, the mechanism at which the molten particle adheres to the substrate is primarily mechanical.

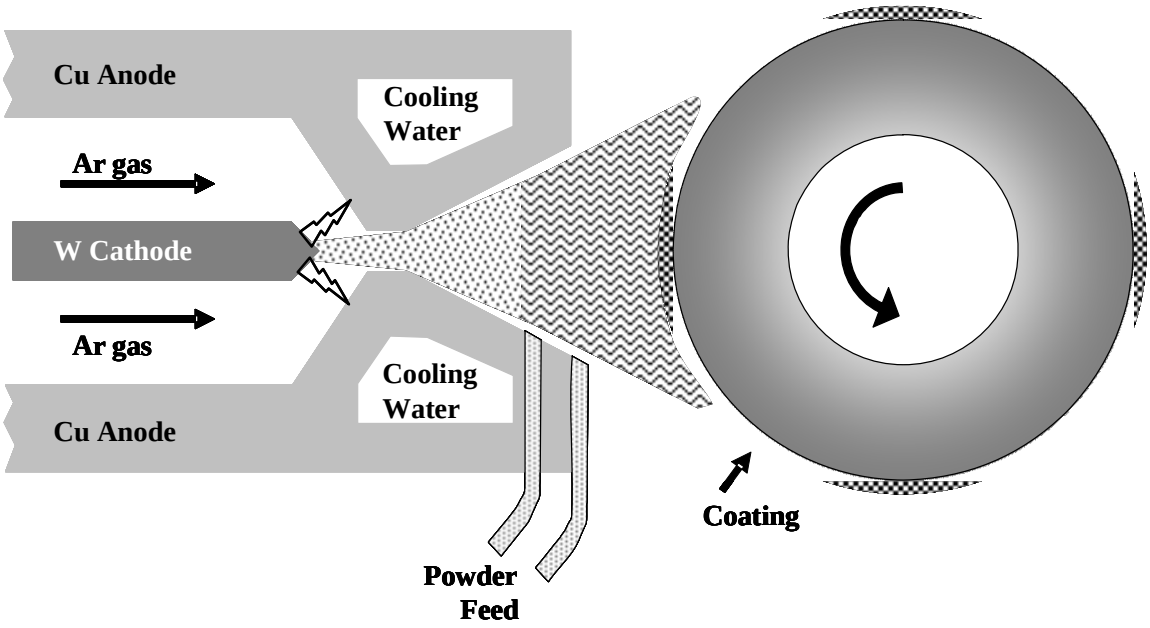

Figure 3. A schematic diagram of the plasma spray gun depicts the application process: an inert gas, such as Ar flows between the cathode and anode; the gas is ionized by an electric arc between the electrodes and forms a high-pressure-gas plasma; powder is fed into the gas stream where it is heated and accelerated by the plasma; the molten powder droplets collide with the substrate, flatten, and cool.

The quality of coating depends on a number of variables: gas flow, power levels, powder feed rate, carrier gas flow rate, standoff (distance between the torch and substrate), angle of deposition, and particle size range, to name a few. The deposition efficiency of the coating is influenced by particle size distribution, rate of heating and acceleration, and also the surrounding atmosphere. Although YSZ is often sprayed in air, it should be noted about the process in general that air can oxidize non-oxide particles which may lead to a decrease in cohesive strength, bond strength, and density. Harmful oxidation effects can be eliminated by spraying in a vacuum or reduced-pressure, inert atmosphere such as vacuum plasma spray (VPS) or low-pressure plasma spray (LPPS). An alternative process for TBC deposition is high velocity oxygen fuel (HVOF) thermal spray,[16] in which the spray gun has the ability to produce an extremely high spray velocity.

The microstructure of an air plasma spray (APS) TBC is shown in Figure 4, displaying a porous, splat-quenched, microcracked structure. The porous microstructure has lamellar layers with macro- and microcracks at splat boundaries. The TBC density is an important parameter within the coating because it is believed that the pores and microcracks contribute to the thermal stress tolerance and low thermal conductivity.

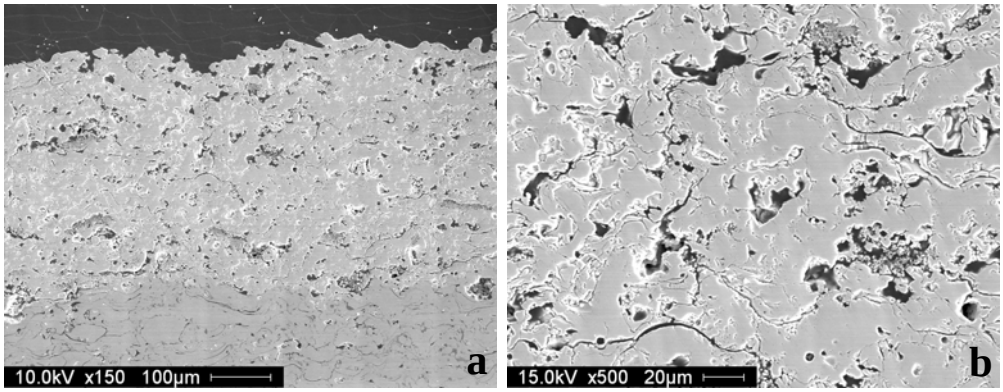

Figure 4. Secondary electron micrographs of plasma sprayed TBC displaying a porous, microcracked structure at (a) 150x and (b) 500x.

2.1.1.2. Electron Beam Physical Vapor Deposition

A second method of applying the YSZ, typically used to coat turbine blades, is electron beam physical vapor deposition (EB-PVD). The microstructure produced by this processing technique, shown in Figure 5, is much different from that of plasma spray, displaying a columnar structure with inter-columnar gaps that provide lateral strain compliance. Each column contains microscopic porosity which reduces the thermal conductivity.

A schematic of this process is presented in Figure 6. Within the evaporation chamber under vacuum in the range of 0.1 to 10 mPa,[17] ceramic pellets with net composition are loaded

into crucibles. High-energy electron beams are used as a heat source to both evaporate the pellets and heat the surface of the blades. The blades are located at an appropriate distance from the vapor source. The vapor flows in a straight line depositing onto the substrate line-of-sight. It is therefore necessary to revolve and rotate the blades within the vapor chamber to produce an even coating on complex geometries.

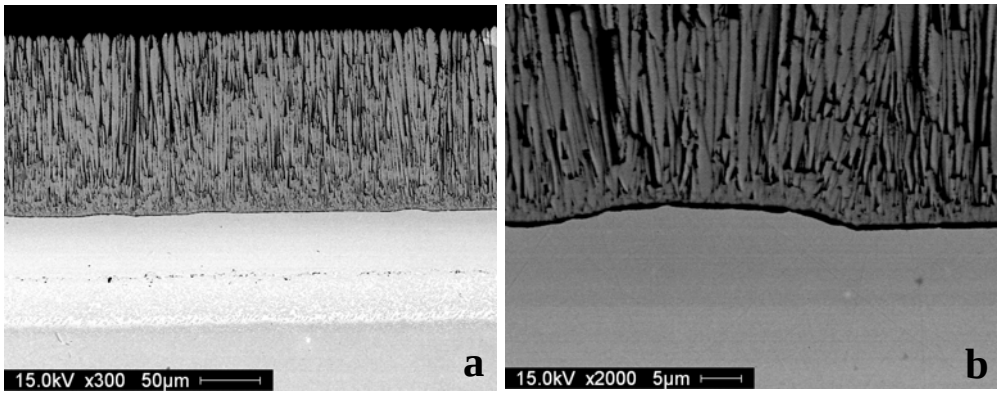

Figure 5. Backscatter electron micrographs of the EB-PVD TBC with (Ni,Pt)Al bond coat at (a) 300x and (b) 2000x.

Heating of the blades during deposition creates an intense heat release from the ceramic layer and creates a thin, fully dense layer of ceramic adjacent to the bond coat. Within the fully-dense layer of ceramic, elements from the bond coat diffuse into the ceramic, atomically bonding the ceramic to the metallic bond coat. This zone has different physical and chemical properties and contributes to the high strength bonding. Above the fully dense zone, a columnar structure of YSZ grows perpendicular to the surface commonly oriented in the [100] direction. This microstructure has improved surface smoothness over the APS, which is one reason it is preferred for turbine blades with aerodynamic considerations.

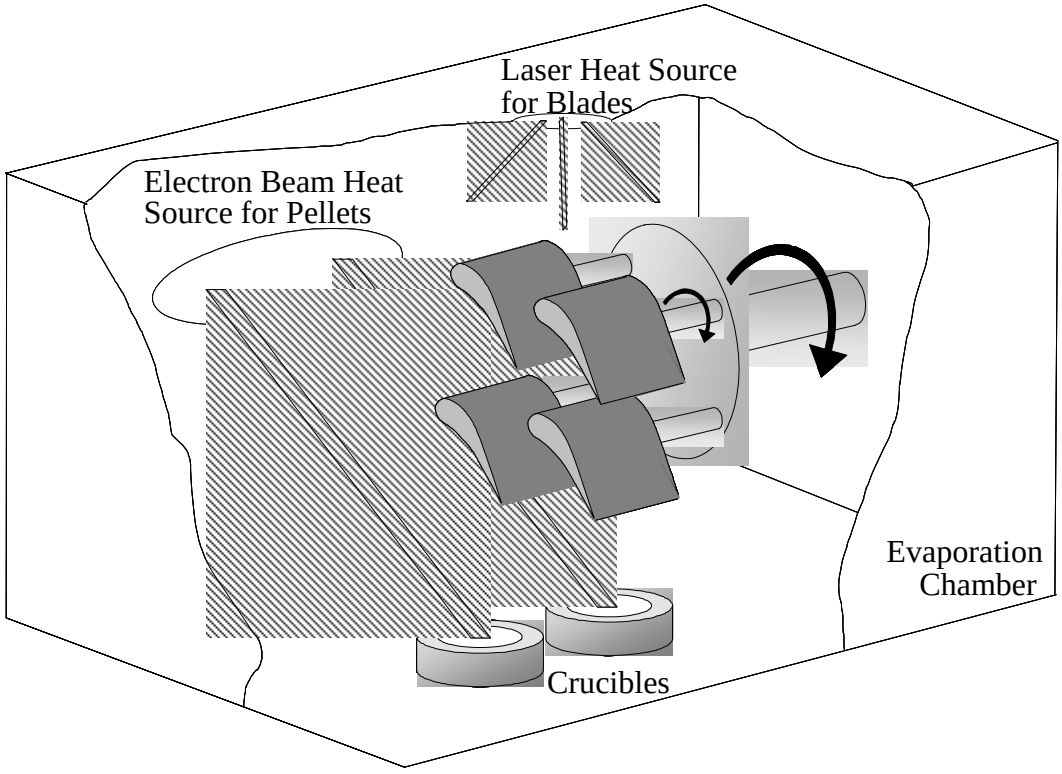

Figure 6. The schematic displays the EB-PVD process, which takes place inside an evaporation chamber: the parts are revolved and rotated while being heated by electron beams; electron beams heat the ceramic pellets in crucibles to form vapor beneath the parts; the vapor deposits onto the heated substrate forming a coating.

The microstructure of the coating is affected by many variables within the processing technique. The ceramic layer structure is dependent not only on the composition of the ceramic pellets, but also on blade surface temperature, condensation rate, and rotation speed of the blades. The surface temperature of the blades affects the thermal stresses within the ceramic layer. The rate of condensation also affects the thermal stresses, as well as the thickness of the crystallites. During deposition, the heating power on the turbine blades must be decreased when condensation begins in order to keep the fully dense zone from growing too thick. Thick layers (>5 μm) may cause black ceramic to form (due to lack of oxygen) in which the monoclinic phase is present. As stated previously, the monoclinic phase decreases the integrity of the coating. A

dense layer of less than 3μm in thickness has been proven to be beneficial and increase the service life of the coating.

2.1.2. Metallic Bondcoat

Prior to the YSZ deposition, a bond coat is applied to protect the metallic substrate from oxidation. Since YSZ is a fast-ion oxygen conductor, without this intermediate coat, oxygen would penetrate the ceramic layer and quickly oxidize the superalloy, forming nickel oxides, nickel-chromium spinels, and chromium oxides which are not thermodynamically compatible with YSZ, and may in turn promote premature spallation of the ceramic layer.

For TBC systems, two types of bond coats are in commercial use: MCrAlY (where M stands for Ni and/or Co) and platinum modified nickel aluminide (Ni,Pt)Al. Both coatings were developed prior to TBCs for oxidation and corrosion resistance for high temperature materials[18] based on the formation of a continuous external layer of alumina (α-Al_2O_3) upon exposure to thermal oxidation (as opposed to formation of internal oxidation). The protective external Al_20_3 scale exhibits low diffusivity of oxygen and phase stability.[19] The objective of the bond coat is to supply aluminum to the thermally grown oxide (TGO) scale that forms on the surface. A reduction in the rate of depletion for Al may lead to prolonged service life of the TBCs.

Processes of MCrAlY coatings include a number of variants of plasma spraying (i.e. LPPS, APS, HVOF, etc.) or by EB-PVD. The overlay coating generally consists of a two-phase microstructure of $\beta + \gamma$ solid solutions. Thick bond coats are achievable with plasma spray coatings that are attractive for its low cost and ability to coat large parts.

At the time, (Ni,Pt)Al coatings were developed as an alternative to MCrAlY coatings for protection at higher temperatures. This diffusion coating is applied, in general, by a chemical

vapor deposition (CVD) process. A layer of Pt is first electrodeposited onto the superalloy substrate. The components are then subjected to an aluminum-rich vapor, in which the aluminum diffuses through the Pt, into the superalloy, and Ni from the superalloy diffuses outward and reacts with the Pt and Al to form the (Ni,Pt)Al aluminide coating. The resulting microstructure is, in general, a single-phase β or a two-phase $\beta + \gamma$ or $\gamma' + \gamma$.

2.2. Failure of Thermal Barrier Coatings

TBCs are not always implemented into design of gas turbine engine components due to uncertain reliability and durability. Coating spallation occurs at or near the TGO interfaces and is preceded by a sequence of events that cause buckling and/or edge delamination. Failure mechanisms as well as reliability differ for different types of TBCs and can vary as a result of application parameters, surface treatments, and thermal exposure.

In a gas turbine engine for land based power generation application, the TBC will endure peak temperatures for long durations (isothermal oxidation). Engines for aero applications run to peak temperature in a cyclic manner for shorter durations. Cyclic oxidation introduces thermal stresses into the coating system primarily from the thermal expansion mismatch between the YSZ topcoat and superalloy substrate (i.e. $\Delta\alpha \sim 5.0 \times 10^{-6}{}^{o}C^{-1}$). It is necessary for the microstructure of the ceramic topcoat to exhibit strain tolerance in order to prevent instantaneous spallation. Application methods for the YSZ has an effect on strain tolerance of the microstructures. For example, APS TBCs form a network of microcracks that break the ceramics into isolated fragments aiding in strain tolerance.[20] EB-PVD TBCs acquire strain tolerance by fragmentizing when tensile stresses arise and from intercolumnar porosity in the

microstructure.[21] As thermal oxidation progresses, desired physical properties of the YSZ are degraded by sintering effects (i.e. healing pores and microcracks and densifying the structure).[22]

For TBC applications, ZrO_2 is stabilized to prevent detrimental t-to-m martensitic phase transformations. Upon high temperature exposure, it is possible for the nontransformable t' phase to decompose into two phases: a low-yttria, transformable tetragonal phase and a high-yttria cubic phase. Upon cooling the tetragonal phase can transform into monoclinic phase at low temperatures, causing a volume expansion of 3-12% that leads to severe cracking in the coating and degradation of mechanical properties. The behavior of phase transformation of partially stabilized zirconia TBC is affected by the chemical composition of the stabilizer and the thermal cycle holding temperature and cooling rate.

The bond coat plays an important role in the degradation of the TBC system. The bond coat provides oxidation protection of the superalloy substrate by supplying aluminum for the formation and growth of an alumina layer during thermal exposure in air. Over time, depletion of aluminum in the bond coat can cause other oxides to form, such as spinels, which oxidize faster and are associated with an increase in volume that can be disruptive and possibly cause lower fracture energies.[23] Also, with the depletion of aluminum, volume changes within the bond coat can occur, forming voids which may be attributed to rumpling of the bond coat surface.[24,25]

The objective of the bond coat during development was to form a protective layer of stable α-Al_2O_3. But upon application of the topcoat, other metastable phases of alumina have been detected by PL and confirmed by TEM. [26,27,28] In addition to a continuous layer of stable α-Al_2O_3 phase (hexagonal-closed packed), metastable phases such as γ-Al_2O_3 (cubic) and/or θ-Al_2O_3 (monoclinic) may be present in a mixed-oxide layer of the TGO consisting of Al_2O_3 and YSZ. With thermal oxidation, these metastable phases transform into α-Al_2O_3. The phase

transformation within the mixed oxide region of the TGO may cause voids near the TGO/YSZ interface and may be attributed to degradation.[29] Grit-blasted bond coats, on the other hand, rapidly form α-Al_2O_3 and exhibit no phase transformations during thermal oxidation.[26,30]

Spallation of the TBC from the substrate is dependent on time at high temperature, number of thermal cycles, and TGO thickness. These factors induce residual stresses in the TGO. Undulations or rumpling along the bond coat/TGO interface results from thermal expansion mismatch. Additional stresses arise as a result of residual tensions normal to the interface as illustrated in Figure 7 at wrinkles, at oxide heterogeneities, and at grain boundary ridges in the bond coat causing preferential crack nucleation.[31,32] Studies of surface treatments to minimize surface roughness prior to the YSZ deposition can prolong the life of the TBC.[33,34] Propagation and coalescence of microcracks lead to eventual spallation.

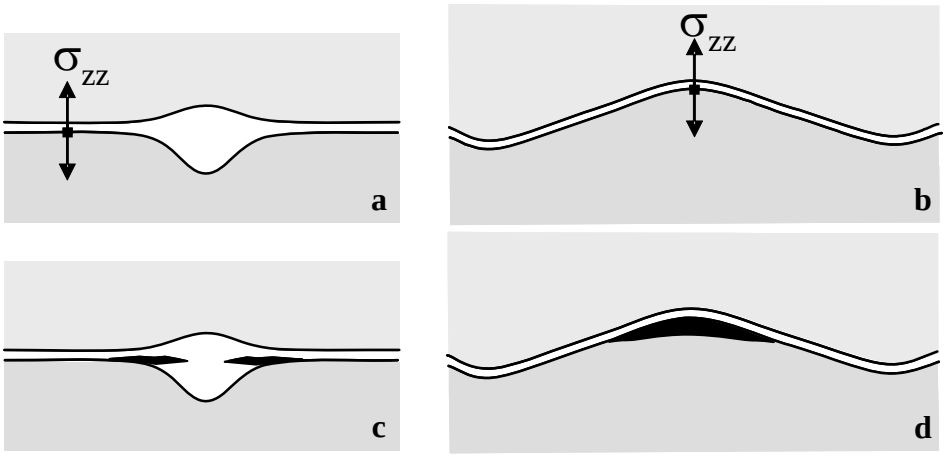

Figure 7. Out-of-plane stresses exist near (a) oxide heterogeneities and (b) at peaks of undulations. Cracks can form (c) within the TGO and (d) at the TGO/bond coat interface as a result of the these stresses.

Buckling spallation is characterized by three non-dimensional indices: the buckling index (Π), adhesion index, and mode mixity index. The buckling index is calculated as follows:

$$\Pi = \left(1 - \nu^2\right)\left(\frac{\sigma}{E}\right)\left(\frac{b}{h}\right)^2 \quad \textbf{(1)}$$

where the interface separation size is b, h is TGO thickness, E is Young's modulus, ν is Poisson's ratio, and σ is the compressive stress. The critical value of the buckling index for buckling to occur is Π_c = 1.22. TBC thickness is typically larger than 100μm, therefore, according to this theoretical model, the critical size of a flaw to induce buckling can be on the order of millimeters.[35] It has been proven that interface separations first form and then grow, but there is an unresolved issue on how this occurs. YSZ suppresses buckling of the TGO. If there are sufficient voids within the TGO, separating it from the YSZ for an area of critical size, it has been proposed that the required critical flaw size should be close to that for the TGO alone.[36]

The most critical part of the TBC system is the TGO. Spallation occurs at or near the TGO interface: in the ceramic near the TGO; at the TGO/YSZ interface; within the TGO; at the TGO/bond coat interface. Damage evolution occurs by crack nucleation at imperfections at or near the TGO (governed by energy release rates) leading to crack propagation and coalescence until a delaminated area reaches a size large enough to initiate buckling or edge delamination. Recent studies have shown that delamination and buckling occur only toward the end of life and have a very short lifespan. The lifetime of TBCs is dominated by microcracking in the TGO. Thermal images were evaluated for an EB-PVD specimen upon cooling. After 20 minutes, a small delamination 1.4 mm in diameter was observed. At a rate of 1.46 mm/min, the

delamination propagated in preferential directions in a “telephone cord” morphology. Once the delamination reached a critical size (i.e. 4.27mm), the ceramic topcoat buckled. The critical size of the delamination corresponded to the thin film buckling theory, where the critical size for buckling was calculated with Eq. 1 to be 4.06 mm.

In the present work, failure mechanisms have been systematically investigated for both APS and EB-PVD coating systems and will be discussed in detail for each type.

2.2.1. Air Plasma Spray

The bond coat surface is typically rough, and is modeled in a wavy fashion in Figure 8(a) for an alumina scale with no TBC. Tensile and compressive stresses develop in the TGO at the peaks and valleys, respectively. The stress distribution in the TGO at the peak of the undulation causes separation between the TGO and bond coat as illustrated in Figure 8(b).[37]

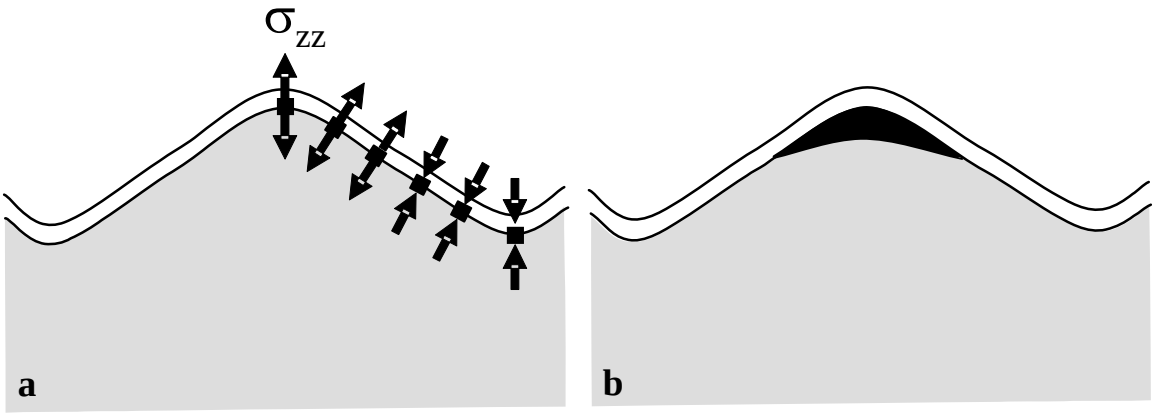

Figure 8. For an alumina scale on a bond coat with no YSZ topcoat, (a) stresses normal to the interface are tensile at the peaks of undulations and compressive in the valley. (b) The distribution of residual stress causes separation between the TGO and bond coat interface at the peaks.

With an applied APS TBC topcoat, stresses arise during high temperature exposure as a result of TGO growth and thermal mismatch during cooling. The stress distribution is similar to the uncoated bond coat depicted in Figure 8(a). Tensile stresses at peaks of the wavy interface are affected by TGO growth. Increasing out-of-plane stresses produce separations at the peaks of waves between the TGO and bond coat.

Thermal expansion mismatch upon cooling causes compressive stresses within the YSZ topcoat. With thermal cycling, the effects of sintering also decrease the strain tolerance in the topcoat. The stresses within the YSZ are an order of magnitude lower than the residual stresses in the TGO. The stress distribution in the TGO (i.e. tensile stress at peaks and compressive stress at valleys of the interface) results in the formation of mesocracks within the YSZ by a brittle or cleavage process and is shown schematically in Figure 9. Out-of-plane stresses are strongly affected by TGO thickness and sintering of the topcoat, whereas the ratio of width to height of the wavy interface morphology has less influence in the formation of mesocracks.[38,39,40]

The coalescence of mesocracks with TGO/bond coat separations creates through-thickness cracks in the TGO, shown in Figure 10.[41,42] Propagation of these cracks occurs particularly during cooling parallel to coating surface at areas of high residual stress.[43]

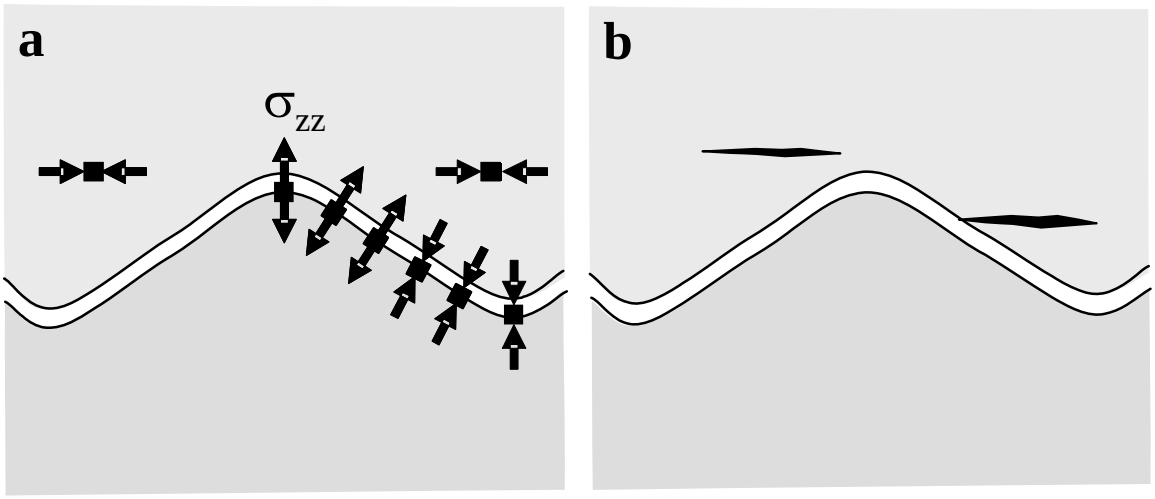

Figure 9. (a) The stress distribution in the TGO of an APS TBC is tensile at the peaks and compressive in the valleys of the wavy interface due to oxide growth. The YSZ exhibits compressive stresses due to thermal mismatch. (b) As a result of the stress distribution, mesocracks can form in the YSZ near the TGO/YSZ interface.

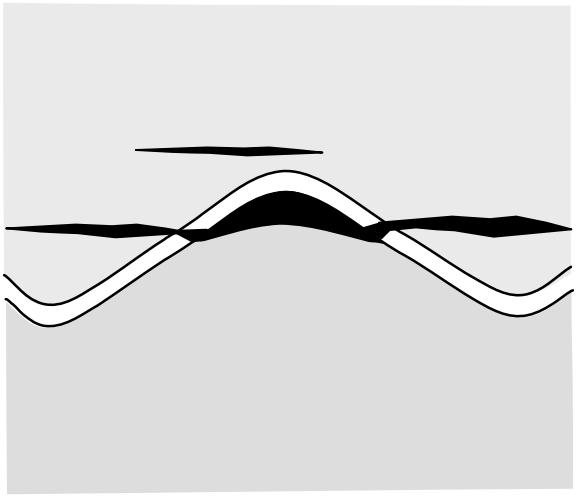

Figure 10. In an APS TBC system, through-thickness cracking of the TGO occurs by linking of the mesocracks with the bond coat/TGO separations. Propagation and coalescence of these cracks leads to final spallation.

2.2.2. Electron Beam Physical Vapor Deposition

EBPVD TBCs may exhibit roughening or rumpling of the bond coat/TGO interface as a result of thermal expansion mismatch. Separations at the peaks of undulations of the bond

coat/TGO interface occur as a result of tensile stresses. The rough interface of an MCrAlY bond coat may cause localized cracking within the TGO/YSZ interface or within the YSZ. After depletion of the Al-rich β-phase in an MCrAlY bond coat, Ni and Co oxides form causing voids at the bond coat/TGO interface, degrading its integrity.[44]

Failure mechanisms of EB-PVD TBCs differ for aluminide bond coats compared with MCrAlY. Grain boundaries resulting from aluminizing play a key role in degradation of TBCs. With thermal cycling, grain boundary ridges exhibit in-plane and out-of-plane stresses. Cracks form in the TGO near ridges, allowing oxygen to penetrate into the bond coat and increasing the local Al depletion. Plastic deformation of the bond coat due to thermal expansion mismatch between the TGO and bond coat forms cavities at the grain boundary during cooling. Failure occurs because the cavities and cracking around grain boundaries leads to a smaller intact area with higher stress concentration as well as increased strain energy from oxide growth.[45] Coalescence of cracks lead to final spallation by buckling.

2.3. Non-destructive Evaluation Techniques

NDE techniques are a critical part in the assessment of coating quality prior to and during the life of the coatings. Two NDE techniques were examined in this study for quality control and health monitoring of TBCs: thermal wave imaging and photostimulated luminescence spectroscopy.

2.3.1. Thermal Wave Imaging

TWI is a practical tool for non-destructive evaluation of thermal barrier coatings, due to the quick response and non-intrusive capabilities. This technique basically uses an infrared

camera to record the temperature decay of the specimen surface following a pulse of heat. The pulse of heat diffuses through the specimen, rapidly changing the surface temperature of the material. Although mostly a conduction process, some heat transfer also occurs through radiation and convection. In the presence of a delamination, depicted in Figure 11, the heat diffusion above the defect becomes complex, causing the surface temperature to be higher than the surrounding, intact area. Pulse thermography (PT) is a "boarder technique," appropriate for TBCs since the coatings are relatively thin.

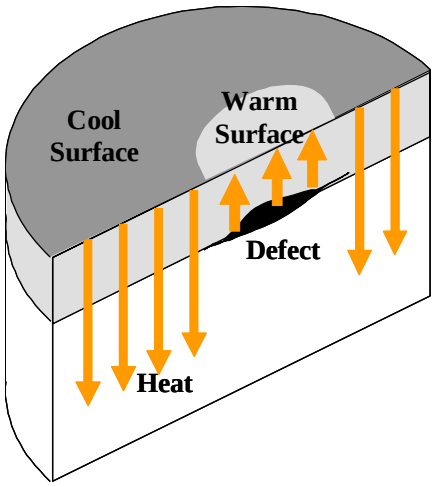

Figure 11. Heat from the thermal flash will diffuse through the specimen. In the presence of a subsurface defect, the thermal wave echoes back to the surface, creating a higher surface temperature above the defect in comparison to the surface above the intact coating.

The TWI system used in this investigation, Ecotherm™, utilizes xenon flash lamps as a heat source to thermally inject specimens with a pulse of heat. An infrared camera, operating within the 6-9 μm spectral region (thermal infrared), captures the real-time surface temperature distribution of the specimens at a rate of 60 frames/second. According to the signal from the raw IR image, the system converts surface temperature per pixel to thermal response amplitude, a unit-less value with a resolution of 1 pixel or ~0.5 mm. The apparatus is shown schematically in Figure 12.

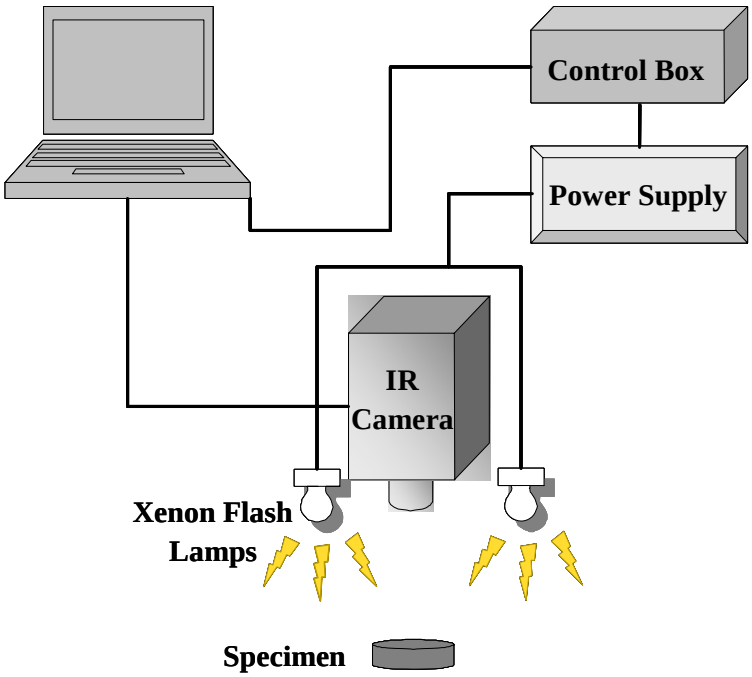

Figure 12. A schematic of Ecotherm™ thermal wave imaging system depicts the collection process: xenon flash lamps provide the heat source; as heat diffuses through the specimen, the infrared camera captures the changes in surface temperature over time (~6 seconds).

For TBCs, the pulse of heat diffuses through the specimen, and the thermal response over a small duration of time (~6 seconds) can give insight to the integrity of adhesion between oxides (e.g., the YSZ and TGO layers) and metallic substrate (e.g., bond coats and substrate alloys).[10,11,12] During TWI, heat transfer within a solid specimen follows the law of conduction expressed by:[46]

$$T(x,t) = \frac{Q}{\rho c (4\pi\alpha t)^{1/2}} e^{\frac{-x^2}{4\alpha t}} \qquad t > 0 \qquad \textbf{(2)}$$

Under the initial and boundary conditions of an infinite plate

$$T(x,\tau) = 0 \qquad t = \tau \tag{3}$$

$$T(\infty,t) = 0 \tag{4}$$

$$\frac{\partial T(0,t)}{\partial x} + HT(0,t) = 0 \tag{5}$$

where T is the temperature that is a function of depth (x) and time (t). Q is the amount of heat created by the source. Materials properties ρ, c, and α refer to density, specific heat capacity, and thermal diffusivity, respectively. The surface temperature (when x = 0) following the thermal injection can be expressed by:

$$T = \frac{Q}{\rho c(4\pi\alpha t)^{1/2}} \tag{6}$$

Eq. 6 can be rewritten as:

$$\ln[T] = \ln\left[\frac{Q}{\rho c}\right] - \frac{1}{2}\ln\left[4\pi\alpha t\right] \tag{7}$$

In the case of TBCs, thermal diffusion must occur through insulating oxides (e.g., YSZ and TGO) and conductive metals (e.g., bond coats and superalloys). Thus, thermal contact resistance between these two layers can give rise to differences in heat flux depending upon the interfacial integrity.[10,12,47] Defects, cracks, and delaminations are commonly observed at or near

this interface and the heat transfer rate locally decreases (i.e., reduced heat dissipation through metallic substrates), causing the surface temperature of the YSZ topcoat to be higher than the undamaged region.[10,12,48,49,50] The temperature discontinuity in the nonideal interface between oxides (T_o) and metals (T_m) can be expressed as:

$$T_o - T_m = R_C Q \quad \textbf{(8)}$$

where R_C is the thermal contact resistance. Large damages between the oxides and metals can create a temperature discontinuity which causes the heat flux through the oxide to decrease.[12,47] The thermal conduction through the YSZ may also be influenced by radiation.[50,51] It is known that YSZ is semi-transparent to radiation within the specified spectral region, but this aspect will not be considered in this study.

2.3.2. Photostimulated Luminescence Spectroscopy

The ability to measure residual stresses in α-Al_2O_3 by piezospectroscopy was developed by Grabner in the 1970's.[52] Based on similar principles, photostimulated luminescence spectroscopy was later developed by Clarke et al.[35,53,54,55,56,57] and refined by Sohn, Gell, Jordan et al. [58,59,60,61,62,63] as a non-destructive evaluation technique for TBCs. This technique has the capability to provide information associated with failure of TBCs in the TGO scale buried beneath the YSZ topcoat, such as residual stresses of α-Al_2O_3, phase constituents, polymorphic transformation, and formation of other oxides (containing Ni, Co, Y, etc.). Application of an excitation source, such as monochromatic light at a particular frequency in the ultraviolet or

visible region, irradiates the ions (or molecules) in the material. The vibrational frequencies of the ions (or molecules) are observed as Raman shifts from the incident frequency.[64]

For a TBC system, a schematic for PL is shown in Figure 13(a). A monochromatic light penetrates the partially translucent YSZ and induces fluorescence of trace amounts of substitutional Cr^{3+} ion impurities in the thermally grown Al_2O_3 scale. Photon emission from Cr^{3+} impurity ions occurs when Al_2O_3 is excited by the laser. The fluorescence is detected as characteristic ruby R-line fluorescence. The spectrum from stress-free polycrystalline α-Al_2O_3 consists of fluorescence doublets R_1 and R_2 at frequencies $14402cm^{-1}$ and $14432cm^{-1}$, respectively, displayed as the dashed line in Figure 13(b). Strain induced on the crystal field around the chromium impurity creates the piezo-spectroscopic effect; a systematic shift in fluorescence frequency of the R-lines displayed as a solid line in Figure 13(b). Measurement of the frequency shift ($\Delta\nu$) can be used to determine the residual stress value in the TGO scale, based on the following relation:

$$\Delta\nu = \Pi_{ij}\sigma_{ij}^{c} = \Pi_{ij}a_{kl}a_{lj}\sigma_{ijkl}^{c} \tag{9}$$

The term Π_{ij} represents the ij^{th} component of the piezo-spectroscopic tensor. The state of stress in the host crystal, dependent on crystallography, is represented by σ_{ij}^{c}. This term can be related to a general coordinate system through the transformation matrix a_{ij} to obtain the stress state (σ_{ij}) independent of crystallography. In PL measurements of polycrystalline alumina, it is assumed that the probe area is much larger than the grain size, the material is not textured and has random crystallographic orientation. By averaging Eq. (9) over all possible crystallographic

orientations, the mean shift in frequency can then be found, in which the shift is dependent only on the hydrostatic component of the applied stress tensor expressed by:

$$\overline{\Delta\nu} = \frac{1}{3}\Pi_{ij}\sigma_{ij}^{mis} \quad \textbf{(10)}$$

It can also be assumed that the TGO scale in the TBC system is affected by biaxial thermal residual stresses, in which $\sigma_{xx} = \sigma_{yy} \equiv \sigma_R^{mis}$. The hydrostatic component of the applied stress tensor can then be expressed in terms of the average residual stress from thermal mismatch (σ_R^{mis}) as:[54,57,65,66]

$$\overline{\Delta\nu} = \frac{2}{3}\Pi_{ij}\sigma_{R}^{mis} \quad \textbf{(11)}$$

During thermal oxidation, cracking within the TGO causes stress relief of the residual stresses.[56,57,60,63] Also, other phases of the TGO scale may be identified in the PL spectra. The luminescence display N, Q, and G-luminescences, indicate significance of Cr_2O_3 concentration in the TGO[67], the presence of metastable θ, and γ-Al_2O_3 in the TGO. Relative intensity of the luminescences can be determined with the following relation:

$$\frac{I_R}{I_T} + \frac{I_N}{I_T} + \frac{I_Q}{I_T} + \frac{I_G}{I_T} = 1 \quad \textbf{(12)}$$

where I_T is the total luminescence intensity of all the integrated luminescence intensities I_R, I_N, I_Q, and I_G from α-Al_2O_3, N-luminescence, θ-Al_2O_3, and γ-Al_2O_3, respectively. PL may have the ability to detect the formation of other constituents in the TGO such as Y-rich oxide (e.g., YAl_5O_{12}, Y_2O_3), and Ni/Co-rich oxide (e.g., NiO, CoO, $(Ni,Co)(Cr,Al)_2O_4$-spinel).[68] With the ability of PL to non-destructively identify these TGO characteristics as a function of thermal cyclic oxidation, this NDE technique can provide insight to failure mechanisms of TBCs specifically associated with polymorphic transformation of Al_2O_3 in TGO, residual stress in α-Al_2O_3 TGO, formation of Ni/Co rich TGO, and adhesion integrity of TGO/bond coat interface.

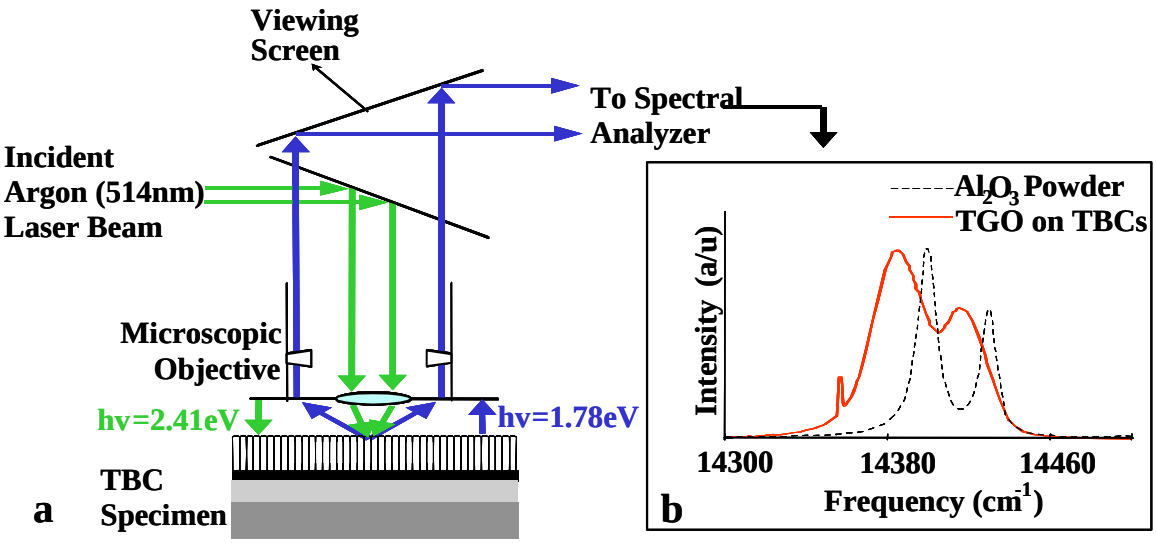

Figure 13. (a) A schematic diagram is shown for photostimulated luminescence spectroscopy and (b) typical spectra for R_1-R_2 luminescence doublets for polycrystalline α-Al_2O_3 (dashed line) without any residual stress and from α-Al_2O_3 scale under compressive residual stress (solid line).

3. EXPERIMENTAL DETAILS

3.1. Specimen Description

Two groups of specimens were studied in this experimental investigation. All TBC analysis was performed on button-shaped TBC samples (25.4 mm in diameter and ~3.2 mm in height). Specimen details will be discussed individually for two experiments.

3.1.1. Air Plasma Sprayed Thermal Barrier Coatings

A total of 13 button samples were produced from Haynes-230 superalloy (Ni-5Co-22Cr-2Mo-14W-3Fe-0.4Si-0.1C) substrate. They were bond coated by APS with NiCoCrAlY (200μm in thickness) at a proprietary* composition. The topcoat was applied by APS with 7-8 wt.% YSZ. The topcoat thicknesses are reported in Table 1.

Table 1. The number of specimens with specified coating thicknesses for APS TBCs.

Number of Specimens	Bond Coat Thickness	YSZ Thickness
9	200μm	380μm
2	200μm	635μm
2	200μm	1015μm

* Solar Turbines Incorporated, San Diego, CA

3.1.2. Electron Beam Physical Vapor Deposited Thermal Barrier Coatings

Eight specimens were coated with 7-8 wt.% YSZ by EB-PVD to a thickness of 145 μm. The CMSX-4 superalloy substrate had a 50 μm-thick (Ni,Pt)Al bond coat prior to TBC deposition.

3.2. Furnace Thermal Cycling Test

Specimens underwent thermal cyclic oxidation in a CM™ Rapid Furnace. The thermal cycle for the APS TBCs differed from the EB-PVD TBCs as will be described.

3.2.1. Air Plasma Spray

Nine APS TBC specimens with YSZ thickness of 380μm were exposed to thermal cyclic oxidation at a peak temperature of 1150°C (2100°F). Each thermal cycle consisted of a half-hour ramp to 1150°C, 10-hour hold at 1150°C, a half-hour air-quench and 1-hour dwell at room temperature.

3.2.2. Electron Beam Physical Vapor Deposition

A total of seven EB-PVD TBC specimens underwent thermal cyclic oxidation. The thermal cycle consisted of a 10 minute heat-up to 1121°C, 40 minute dwell at peak temperature, and 10-minute forced air quench at room temperature. Two of the specimens were then thermally cycled to 10% and 70% lifetimes which correlate to 45 and 280 thermal cycles. These two specimens along with one specimen in the as-coated condition were employed for microstructural evaluation.

3.3. Non-destructive Evaluation

In the as-received condition and during thermal cycling, specimens were removed from the furnace for non-destructive evaluation by either PL or TWI. Table 2 displays the specimen types with corresponding NDE method, cyclic lifetime, and cycles at which specimens were removed for NDE observation.

Table 2. The average lifetime, NDE method, and cycles for NDE observation are presented for each TBC system.

Specimen Topcoat	Topcoat Thickness	Number of Specimens	Average Lifetime (cycles)	NDE Method	Observation (cycles)
APS	**380μm**	**9**	**99 ± 14**	**TWI**	**0, 22, 40, 58, 70, 94, 102, 106 cycles**
APS	**635μm**	**2**	**N/A**	**TWI**	**0 cycles**
APS	**1015μm**	**2**	**N/A**	**TWI**	**0 cycles**
EBPVD	**145μm**	**5**	**406 ± 22**	**PL**	**1, 5, 10, 50, 100, 150 cycles…failure**

3.3.1. Thermal Wave Imaging

The thermal wave imaging system used in this study was by Thermal Wave Imaging, Inc. The heat sources for thermal injection were 2 xenon flash-lamps placed on either side of the camera. Images were collected at a rate of 60Hz for ~6 seconds. All specimens were analyzed in the as-received condition and thermally cycled specimens were analyzed after 22, 40, 58, 70, 94, 102, and 106 cycles. After specific thermal cycles, intact specimens were removed from thermal cycling for microstructural investigation.

The thermal wave images and thermal response profiles for each TBC specimen were analyzed with Ecotherm™ 6 software. Line-analysis across 20,750μm (45 pixels) in length was performed through the center of each specimen. This length eliminates the edge-effect caused by the geometry of the button sample. Three TBC specimens in the as-coated condition with the

YSZ thicknesses of 380μm, 635μm, or 1015μm were examined to assess the thermal wave response of YSZ coatings as a function of thickness. Variation in amplitude of the thermal wave response was examined as a function of acquisition time after thermal injection. The optimum acquisition time after thermal injection was identified as 0.37 seconds for studying thermally cycled TBCs.

3.3.2. Photostimulated Luminescence Spectroscopy

PL spectra were collected using Renishaw™ 1000B μ-Raman spectrometer, a compact laser Raman microprobe/microscope with a personal computer interface for instrument control. Optical signals produced by the sample (i.e., fluorescence) were detected after analysis by a grating lightpath through a sensitive charged coupled device (CCD) array detector.

Spectral collection and analysis was performed using Galactic GRAMS™ software. This software used a non-linear least squares curve-fitting routine for a mix of Lorentzian and Gaussian functions.[35,69,70] Curve-fitting of the spectra from stressed TGO was performed based on parameters set by Nychka and Clarke.[71] A curve-fitting was considered satisfactory when the distance between peaks R_2 and R_1 were between the values of 29 and 35 cm^{-1} ($29cm^{-1} < R_2 - R_1 < 35cm^{-1}$). Also, the integrated intensity ratio of R_2 to R_1 was between the range of 50% and 70% ($50\% < I_{R2}/I_{R1} < 70\%$). According to Nychka and Clarke, the fraction of Lorentzian (the L-fraction) and Gaussian G-fractions (where G = 1-L) for stressed alumina were found to lie in the range of L = .40 – .70 for R_2 and L = 0.70 – 0.90 for R_1.

α-Al_2O_3 without any residual or applied stress produces an R-line ruby doublet, shown in Figure 14 as a dashed line. This spectrum is fit with one set of R_1 and R_2 peaks and iterations were performed until the best fit was obtained with a maximum of 50 iterations. In a TBC system

with the TGO under compressive residual stress, the spectrum shifts to a lower frequency and broadens, as shown in Figure 14 as a solid line. This spectrum, resulting from the TGO with residual stress is not adequately curve-fitted with only one set of doublets. It is therefore necessary to fit the data with 2 sets of doublets (bi-modal curve fit), where both sets satisfy the aforementioned curve-fitting criteria. In some cases, two sets of doublets did not satisfy all the conditions and a third set of peaks was incorporated into curve-fit (tri-modal curve-fit).

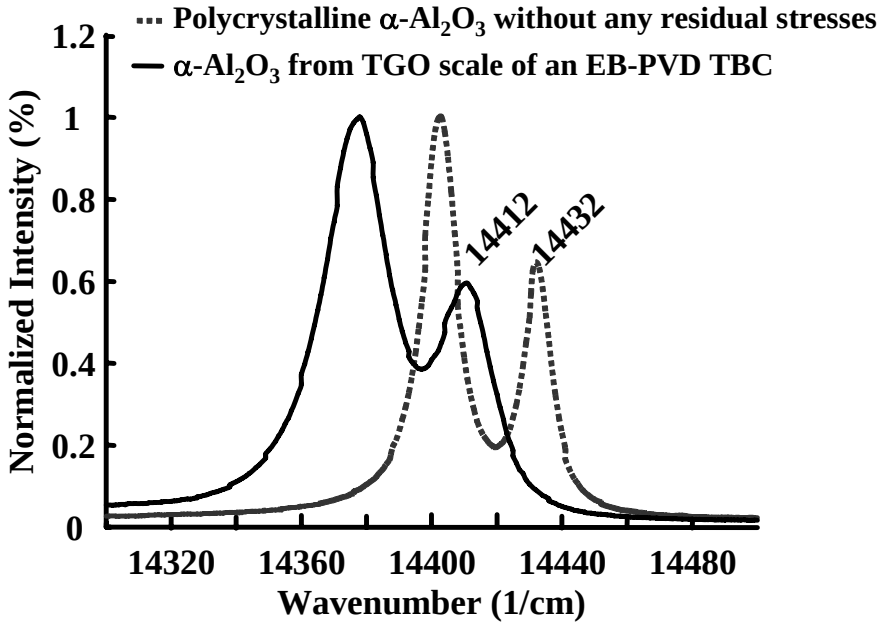

Figure 14. An example PL signal from a TGO scale for an EB-PVD specimen (solid line) is compared with PL signal from polycrystalline α-Al_2O_3 (dashed line) without any residual stress.

The curve fitting process revealed two sets of R_1-R_2 luminescence (denoted R_1-R_2 and R_1'-R_2') for α-Al_2O_3 scale throughout thermal cycling. This bi-modal curve fit is displayed in Figure 15(a), where the set of peaks to the left are designated R_1-R_2 and the set of peaks to the right are referred to as R_1'-R_2'. As previously mentioned, there is a rise in luminescence that

emerges after ~50% lifetime near the stress-free value $\nu \sim 14432$ cm^{-1}. Deconvolution of this type of spectra requires a third set of R_1-R_2 peaks near the stress-free value represented as R_1"-R_2" in Figure 15(b) and is referred to as tri-modal curve-fitting.

In the as-coated condition, these specimens displayed luminescence from metastable phases. During initial cycling, the curve-fitting criteria were not satisfied by bi-modal deconvolution. To obtain an accurate curve-fit, a low-intensity metastable peak was incorporated into the curve-fit at a frequency ~14340 cm^{-1}. Deconvolution of spectra with metastable luminescence during thermal cycling is shown in Figure 15(c), with the metastable peak denoted with an "M." With continued thermal cycling, the intensity of the metastable peak decreased, and disappeared after ~50 cycles.

From Eq. 11, the sums of the coefficients of the stress tensor have been found to be 7.61 and 7.59 GPa for R_2 and R_1, respectively.[72] Stress measurements were calculated from R_2 values and analyzed. The PL data were evaluated for residual stresses in α-Al_2O_3 and polymorphic transformation.

Specimens which underwent 1-hour thermal cycling were analyzed at room temperature with PL at 0, 1, 5, 10, 25, 50, 100, and every 50 cycles until failure occurred. Specimens which were analyzed until 10% and 70% of average lifetimes had PL measurements taken every 20 cycles. Twenty random-spot measurements over the surface of the specimen were analyzed. The light for exciting the Raman scattering and photoluminescence was provided by an Argon ion (Ar^+) green (514.5.2nm) laser operating at 30 mW. At a 5X objective, the spot size for these measurements was very large and may be ~100 μm on the top surface of the YSZ. The effective spot size on the TGO may be greater due to scattering within the YSZ.

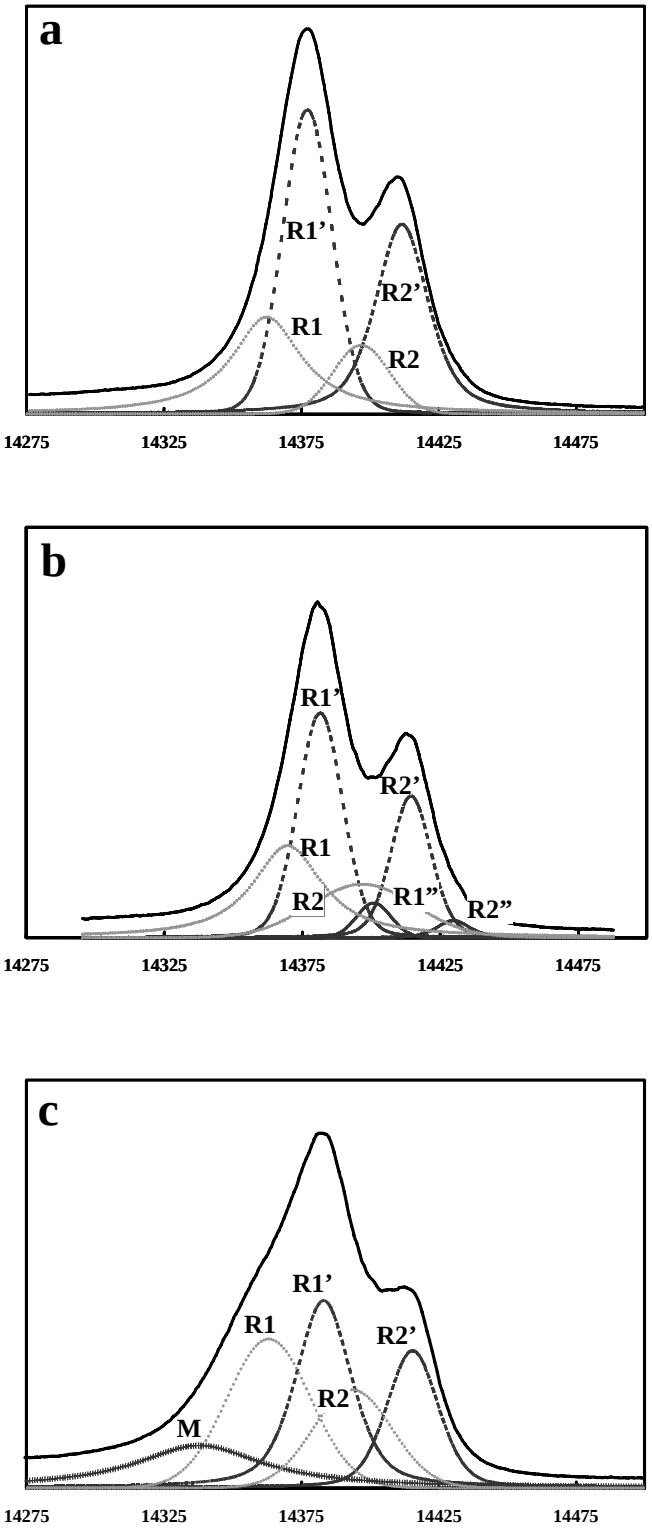

Figure 15. Examples of spectra obtained from EB-PVD specimens are presented with curve-fitting methods: (a) bi-modal, (b) tri-modal, and (c) bi-modal with a metastable luminescence.

3.4. Microstructural Analysis

During and after thermal cyclic oxidation testing, selected specimens of TBCs were selected for the microstructural and failure analysis. The development of microstructural features and failure characteristics of TBCs were examined as a function of thermal cycles. Microstructure and phase constituents of the TGO scale and the fracture surfaces (i.e. the top surface of the bond coat and the bottom surface of the spalled YSZ) were examined by optical microscopy (Nikon HFX-IIA), scanning electron microscopy (SEM) (JSM-6400F) and energy dispersive x-ray spectroscopy (XEDS).

3.4.1. Specimen Preparation

Specimens were initially mounted in epoxy and cross-sectioned with a Buehler™ Isomet™ low speed diamond saw. They were then ground and metallographically polished down to 1 μm. Prior to SEM observation, specimens were coated with a thin layer of carbon for conduction purposes.

Of the 9 APS samples used for thermal cycling and NDE by TWI, five were cycled to failure, while the remaining 4 were removed from the furnace after specified thermal cycling for microstructural evaluation. Table 3 lists the duration of thermal cycling carried out for each sample, and indicates those removed for microstructural characterization.

Table 3. The specified APS TBC samples examined in this study are presented with corresponding number of thermal cycles endured and condition of samples when removed from oxidation. Specified samples were cross-sectioned for microstructural analysis.

TBC Sample ID	Total Thermal Cycling (Cycles)	Condition of TBC Sample	Selection for Microstructural Analysis
9	0	As-deposited	✓
11	102	Failed	
12	106	Failed	
13	106	Intact	✓
14	106	Failed	
15	102	Failed	
16	94	Intact	✓
17	70	Failed	
18	58	Intact	✓

Initially, five EBPVD TBCs were thermally oxidized in 1-hour cycles until failure. After failure, the fracture surfaces (i.e. the bottom side of the YSZ and the top side of the spalled surface of the bond coat) were examined with SEM. The spalled button sample was then mounted and cross-sectioned for microstructural analysis. After the average lifetime of the EB-PVD specimens was determined, two samples from the same batch were oxidized in 1-hour cycles until 10% and 70% life had passed. The specimens were removed from thermal cycling after specified times noted in Table 4 for microstructural analysis. These samples were first non-destructively analyzed with PL to ensure similar NDE characteristics to the set of samples cycled for lifetime determination.

Table 4. EB-PVD TBC samples examined in this study are presented with number of cycles experienced with 1-hour thermal cycling and condition of samples when removed from the thermal cyclic oxidation for microstructural analysis.

TBC Sample ID	Total Thermal Cycling (Cycles)	Condition of TBC Sample	Selection for Microstructural Analysis
1	0	Intact	✓
2 – 6	406 ± 22	Failed	✓
7	45	Intact	✓
8	280	Intact	✓

3.4.2. Scanning Electron Microscopy

Backscatter and secondary electron imaging was performed on a scanning electron microscope. The SEM work in this investigation was performed on a JEOL-6400F equipped with x-ray energy dispersive spectroscopy (XEDS). The apparatus utilizes a cold cathode field emission electron gun and has a resolution of 1.5nm. Images were collected with a voltage ranging from 15.0 to 25.0 kV at a constant emission current of 8μA.

4. RESULTS

4.1. Thermal Wave Imaging

4.1.1. Thickness Measurement of Air Plasma Spray Thermal Barrier Coatings

For the as-coated TBC specimens with varying YSZ thickness (i.e., 380μm, 635μm, and 1015μm), Figure 16 shows thermal wave images collected at 0.25 and 1 second following thermal flash heating by xenon lamps. Thermal wave images obtained at 0.25 second do not show any distinction between the specimens, but those collected after 1 second (e.g., frame 60) do. The specimens with YSZ coatings of 380μm thickness show darker images, indicating lower thermal response amplitude. The heat injection after 1 second had conducted through the thin YSZ and dissipated into the conductive metallic bond coat/superalloy substrate. On the other hand, specimens with 1015μm thickness displayed a brighter image since the heat dissipation through the thicker YSZ coating is incomplete. Cross-sectional optical photomicrographs of these TBC specimens with varying thicknesses are presented in Figure 17.

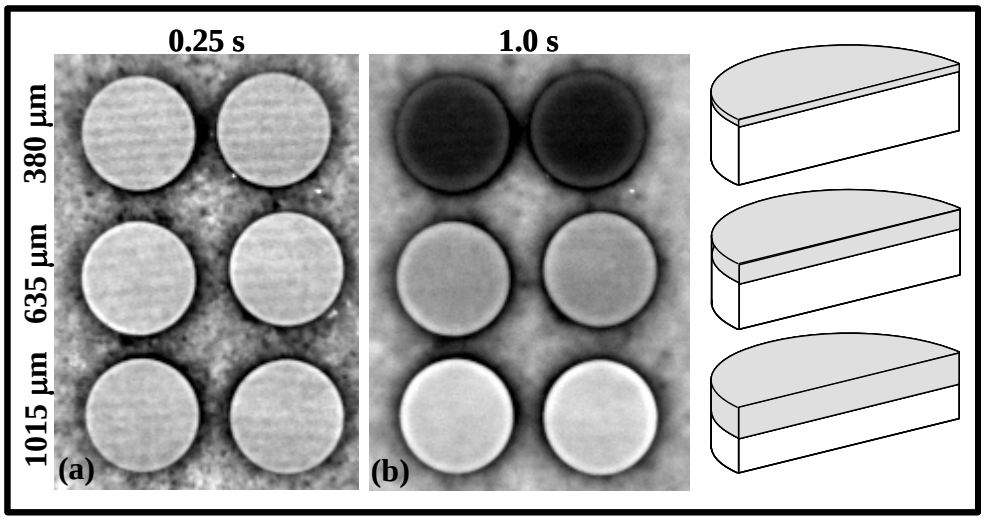

Figure 16. Thermal wave images of APS TBCs coated with varying YSZ thickness at (a) 0.25 second and (b) 1 second following thermal flash heating. A distinction in thermal images as a function of YSZ thickness was observed at 1 second after thermal injection.

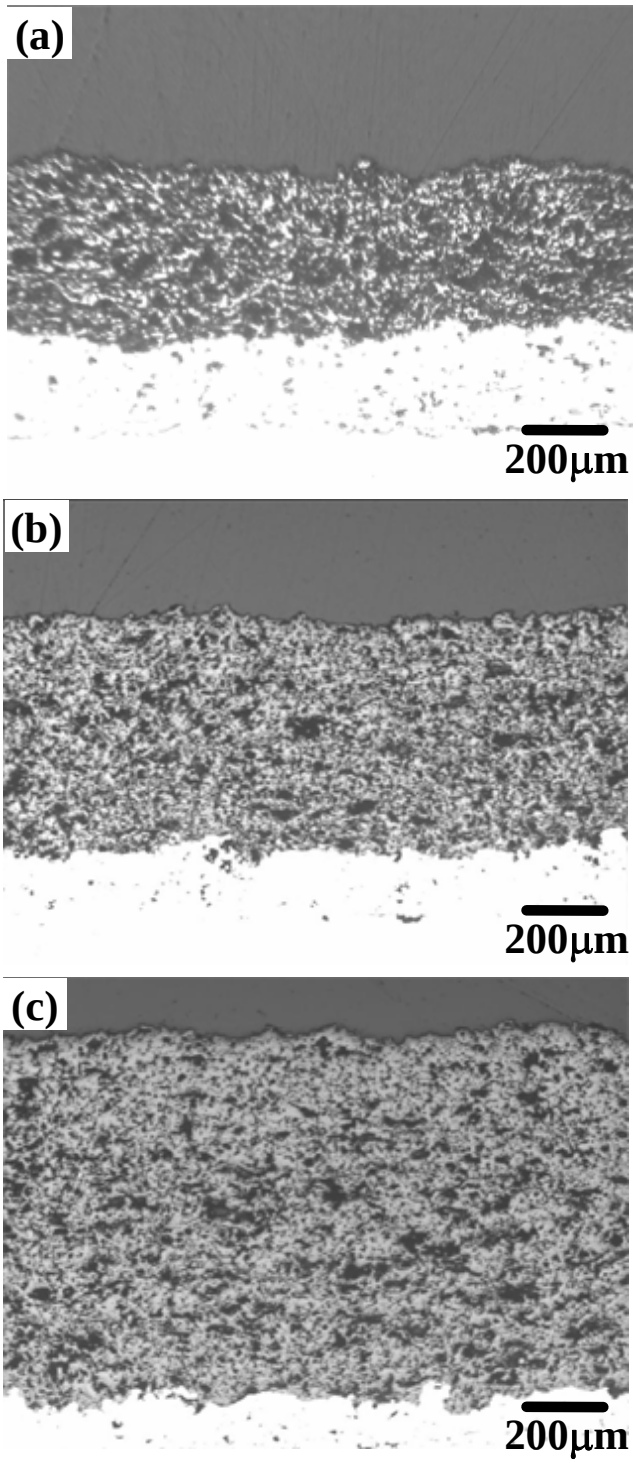

Figure 17. Cross-sectional optical photomicrographs of as-coated TBCs with varying YSZ thickness of (a) 380μm, (b) 635μm, and (c) 1015μm.

4.1.2. Damage Detection for Air Plasma Spray Thermal Barrier Coatings

Thermal wave images from TBC specimens as a function of thermal cycling are presented in Figure 18. These images were acquired at 0.37 seconds following thermal flash heating. Prior to the first thermal cycle at high temperature in air, the images appeared very bright, and exhibited a large amplitude in thermal response.

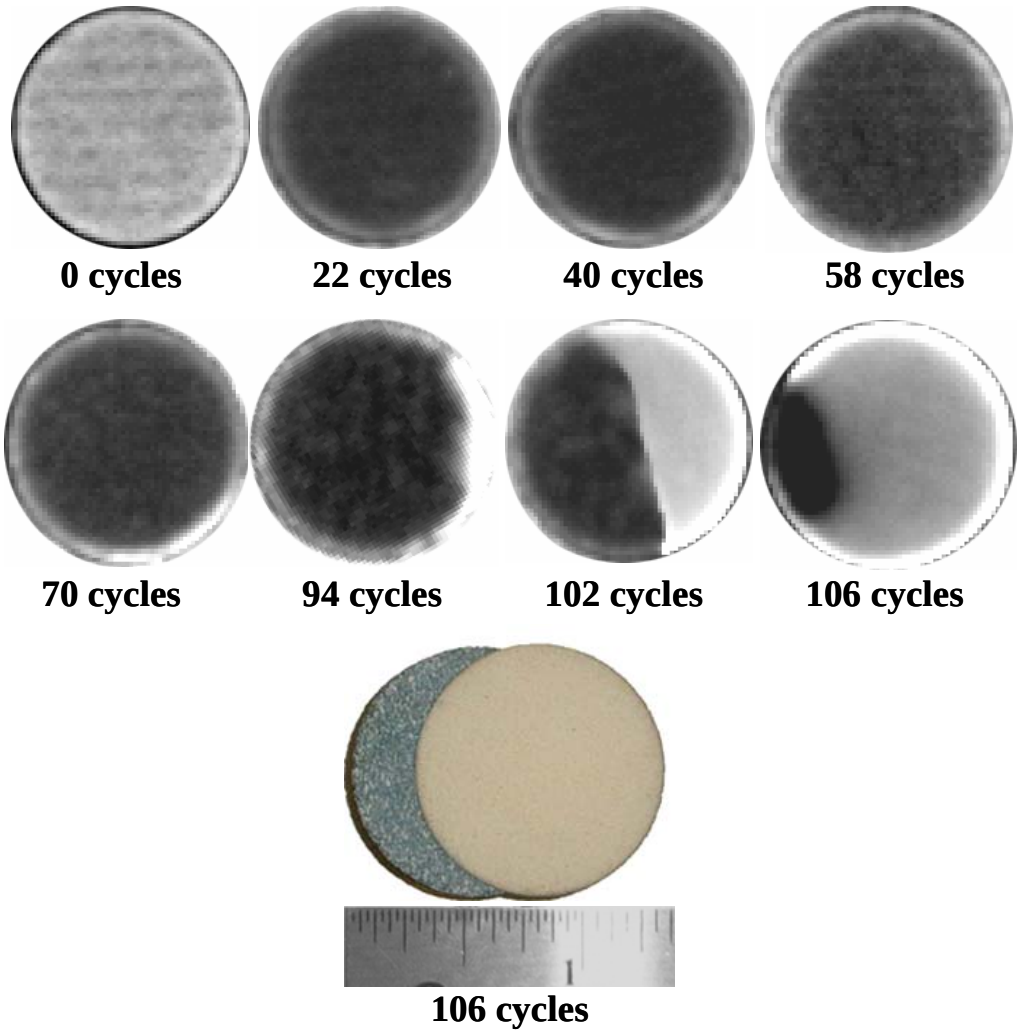

Figure 18. Typical thermal wave images of TBC specimens with 380μm-thick YSZ as a function of 10-hour thermal cycling at 1150°C. Bright regions formed along edges are indicative of subsurface delamination. Final spallation occurred in one piece as shown in the digital photograph.

After initial thermal cycling, thermal wave images of TBCs acquired at 0.37 seconds after thermal injection become darker with a lower amplitude in thermal response. With further thermal cycling, brighter regions began to appear along the edges of the button specimens as a result of edge delamination as shown in Figure 18. The amount of bright region associated with delamination increases prior to the final failure of APS TBCs. The thermal response amplitude averaged over the line analysis as a function of thermal cycling is presented in Figure 19, and compliments the thermal wave images in Figure 18. The thermal response amplitude was initially very high, decreased after thermal oxidation, then gradually increased, before an abrupt increase (i.e. both in magnitude and deviation) due to a development of delaminations.

Small changes in thermal response amplitude occurred between 22 and 58 cycles as shown in Figure 20. A significant rise in the change in thermal response amplitude was observed between 58 and 70 thermal cycles. After 94 cycles, edge delaminations were visible in the thermal images which accounts for the rise in amplitude change and the large standard deviation.

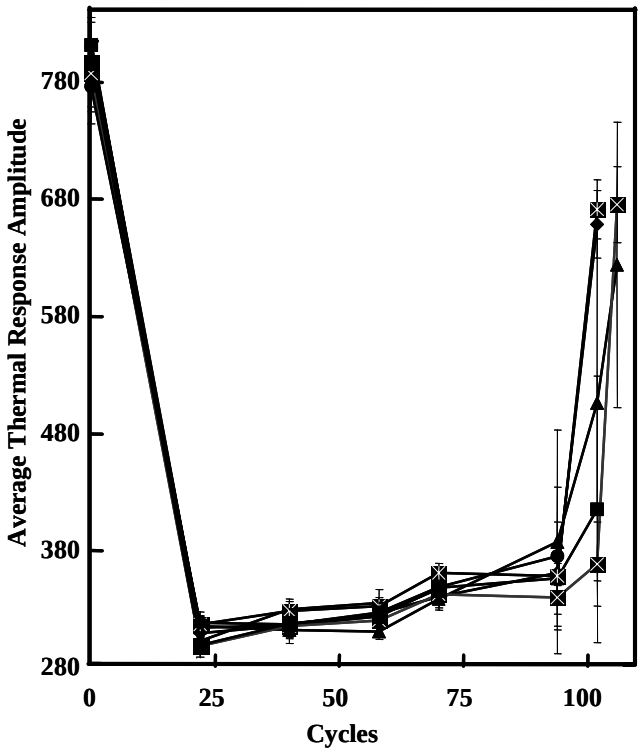

Figure 19. The average thermal response amplitude for APS TBCs as a function of thermal cycling at 1050°C.

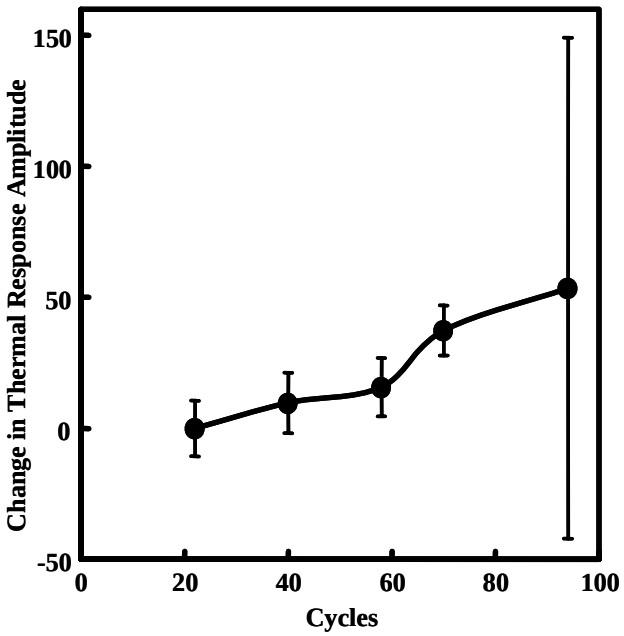

Figure 20. The change in thermal response amplitude of APS TBCs from 22 to 94 cycles.

4.2. Photostimulated Luminescence Spectroscopy

4.2.1. Damage Detection During Cyclic Oxidation for Electron Beam Physical Vapor Deposited Thermal Barrier Coatings

Figure 21 represents typical spectra as a function of 1-hour cycling along with the corresponding second derivatives of the curves. Luminescence intensity is primarily from α-Al_2O_3, indicated by the ruby doublets. Yet in the as-received condition, PL showed signs of θ-phase, indicated by the black arrow in Figure 21. The frequency value of α-Al_2O_3 for R_2 without residual or applied stress (i.e. ν = 14432 cm^{-1}) is specified by a dashed vertical line. A shift in luminescence from this frequency in Figure 21 is associated with compressive residual stress in the TGO. After ~50% lifetime, the spectrum began to show an inflection in the curve near the R-line frequency value ν = 14432 cm^{-1} as a result of a rise in luminescence that is associated with stress-relief of the TGO. The evolution and detection of stress-relief in the TGO can be quantified by examining the first ($dc/d\nu$) and second ($d^2c/d\nu^2$) derivatives of luminescence spectrum (denoted as c) associated with the frequency for luminescence of Al_2O_3 without any stress at ν ~ 14432 cm^{-1} for R_2. The second derivative of the luminescence spectrum (Figure 21(b)) with ($d^2c/d\nu^2$) = 0 at 14432 cm^{-1} ± 3 cm^{-1} displays the emerging inflection of spectra after ~50% lifetime. In some cases, the first derivative of the spectra indicated stress-relief in the TGO: ($dc/d\nu$) = 0 at ν = 14432 cm^{-1} ± 3 cm^{-1}. An example of the raw spectra and first derivative is shown in Figure 22. In this case, the luminescence intensity from the stress-relief dominated the signal from TGO and is quantified by observing the first derivative.

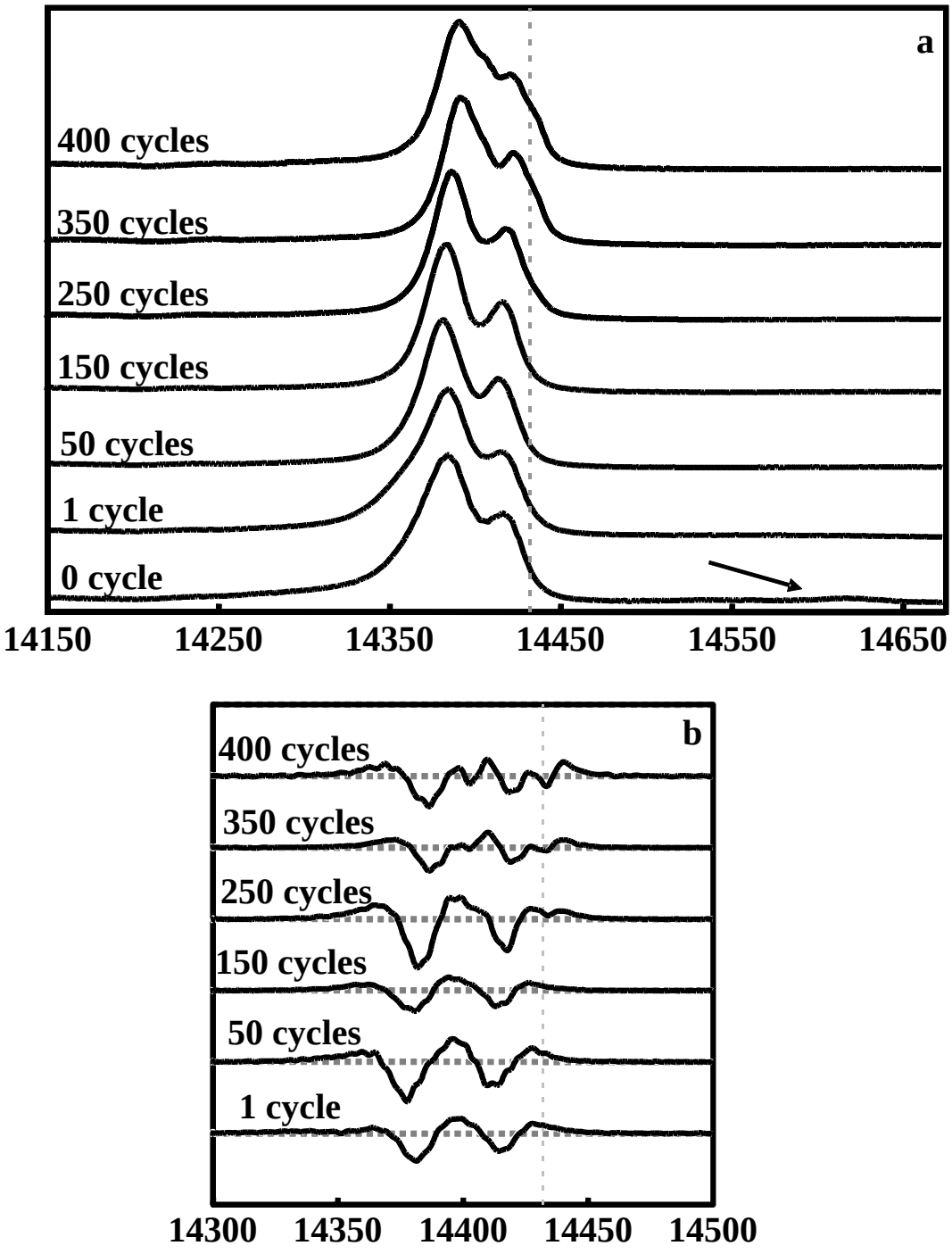

Figure 21. (a) Typical spectra evolution over thermal cyclic oxidation. Metastable phases were initially present as shown by the arrow and (b) the second derivative of the spectra show an evolution of luminescence near the R_2-line for $\nu = 14432 cm^{-1}$.

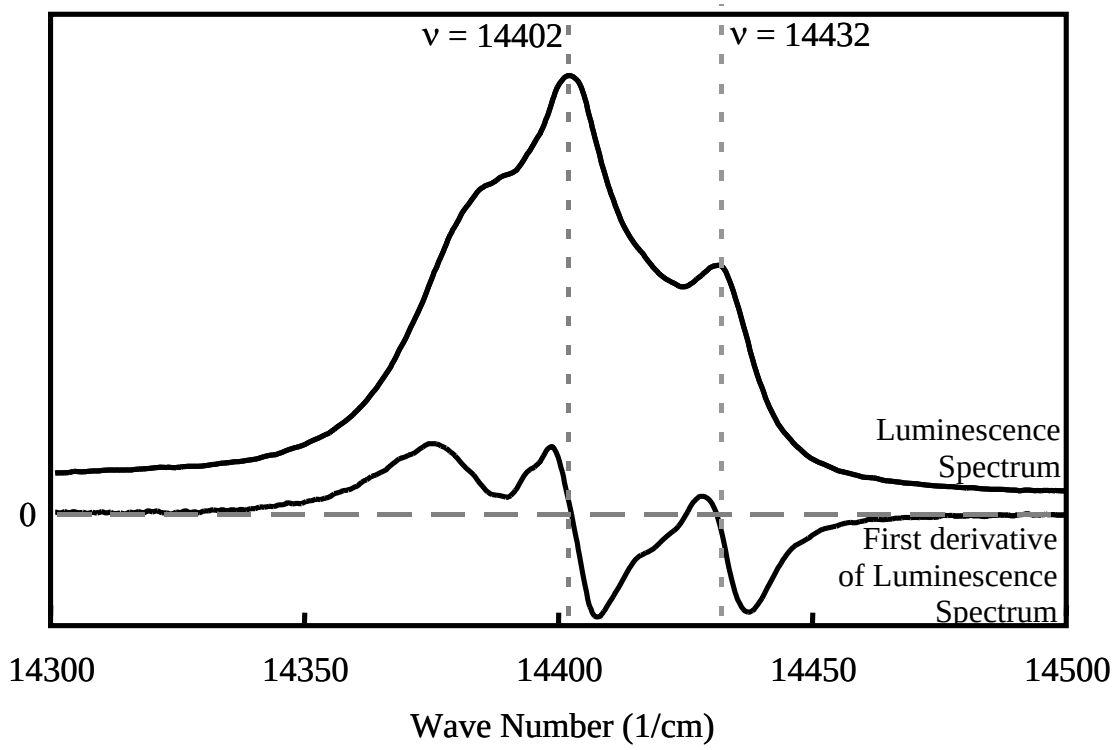

Figure 22. The first derivative with the corresponding spectrum taken after 400 thermal cycles crosses the zero axis at the R-line values for α-Al_2O_3 without any residual stresses (ν = 14402, 14432 cm^{-1}).

As shown in Figure 23, the luminescence spectrum with (dc/dν) = 0 at ν = 14432 cm^{-1} ± 3 cm^{-1} and (d^2c/dv^2) = 0 at 14432 cm^{-1} ± 3 cm^{-1} was observed starting after 200 cycles, and thereafter gradually increased in terms of population out of 20 random-spot measurements with thermal cycling. After 400 cycles, more than half of the 20 randomly selected measurements indicated localized stress-relief associated with damage in the TGO scale.

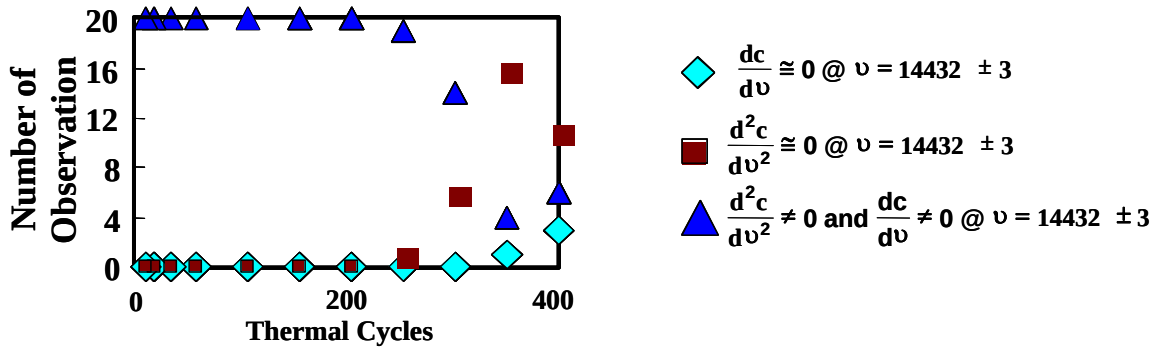

Figure 23. Number of PL spectra that exhibits luminescence from stress-relief according to the first and second derivates as a function of 1-hour thermal cycling for EB-PVD TBCs with as-coated (Ni,Pt)Al bond coats. Luminescence from stress-relieved TGO scale was observed after 50% lifetime and thereafter increases until failure at 420 cycles.

4.2.2. Spectroscopic Analysis

The relative luminescence intensity of the metastable peak and the R_2 intensity from the three α-Al_2O_3 peaks (i.e $I_{metastable}$, I_{R2}, $I_{R2'}$, and $I_{R2''}$) with respect to the total relative intensity (i.e. $I_T = I_{metastable} + I_{R2} + I_{R2'} + I_{R2''}$) is plotted in Figure 24 as a function of thermal cycling. Metastable alumina was initially present and vanished after ~50 cycles. This indicates that the metastable phase transformed into equilibrium α-Al_2O_3 with thermal oxidation, although it is not a quantitative measurement of the actual volume fraction. Another observation from the plot of relative luminescence is the emergence of the stress-free luminescence that began as early as 200 cycles and increased in relative intensity until failure. The emergence of the third set of peaks is an indication of stress-relief in the TGO underneath the YSZ topcoat.

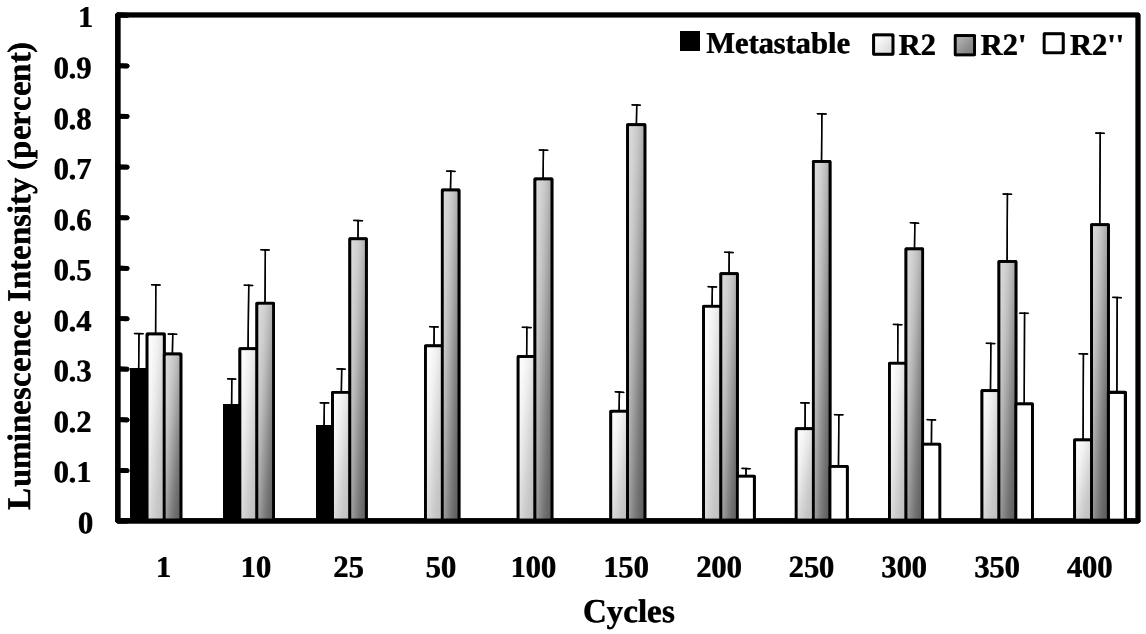

Figure 24. Average relative luminescence intensity as a function of thermal cycling show presence of metastable phases initially, consistent bi-modal luminescence from α-Al_2O_3, and an evolution of a third set of α-Al_2O_3 peaks.

The average compressive residual stress within the α-Al_2O_3 scale as a function of 1-hour thermal cycling is presented in Figure 25. The evolution of compressive residual stress and the emergence of tri-mode luminescence from TGO stress-relief are shown. The compressive residual stress calculated from the luminescence frequency of the R_1-R_2 was unusually high in magnitude. Typically in literature, the highly stressed set of α-Al_2O_3 luminescence is ~6GPa,[54,55,73] whereas the data in this study exhibited stresses as high as 8GPa. This phenomenon may result from bond coat processing. With thermal cycling, a systematic shift in luminescence was observed due to stress-relaxation. The luminescence from stress-relief that emerged after ~50% lifetime displayed very low magnitude of compressive stresses, less than 1 GPa, and remained low until failure.

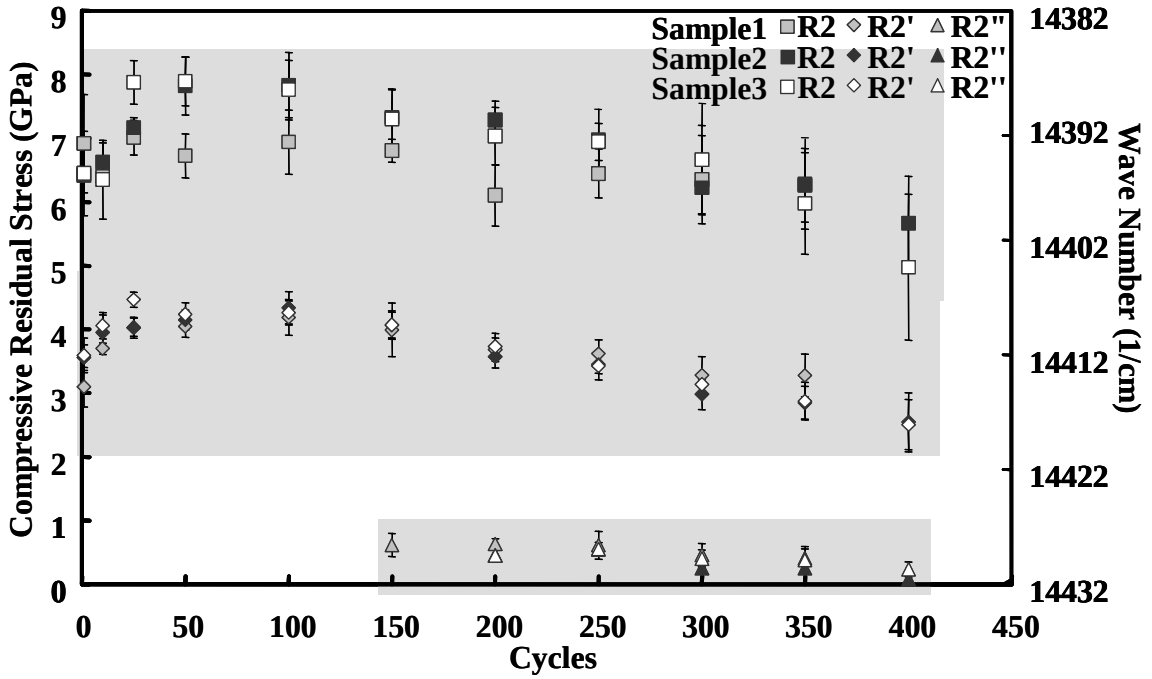

Figure 25. Compressive residual stress within the TGO as a function of 1-hour thermal cycling for EB-PVD TBCs with as-coated (Ni,Pt)Al bond coats. Values of compressive residual stress were calculated from the higher shift luminescence, lower shift luminescence, and luminescence from stress-relief.

4.3. Microstructural Characterization of Thermal Barrier Coatings

4.3.1. Air Plasma Spray Thermal Barrier Coatings

Microstructural analysis was carried out for four in-tact TBC samples removed from thermal cyclic oxidation after 0, 58, 94, and 106 cycles as reported in Table 3. Figure 26 displays the thermal wave images of TBC samples with corresponding cross-sectional backscatter electron micrographs. The thermal wave image of TBC samples after 0 and 58 cycles displayed no indication of damage. The corresponding cross-sectional backscatter electron micrograph for 0 cycles showed no damage. For TBCs with 58 cycles, the coating was well intact with few mesocracks. For the TBC sample with 94 cycles, a few brighter regions in the thermal wave image were observed, while an initiation of damage within the YSZ topcoat near the TGO scale was observed as shown in Figure 26. The in-tact TBC sample with 106 cycles (close to the final

failure) displayed a very high thermal response due to significant damage within the YSZ topcoat near the TGO scale and at the YSZ/TGO interface.

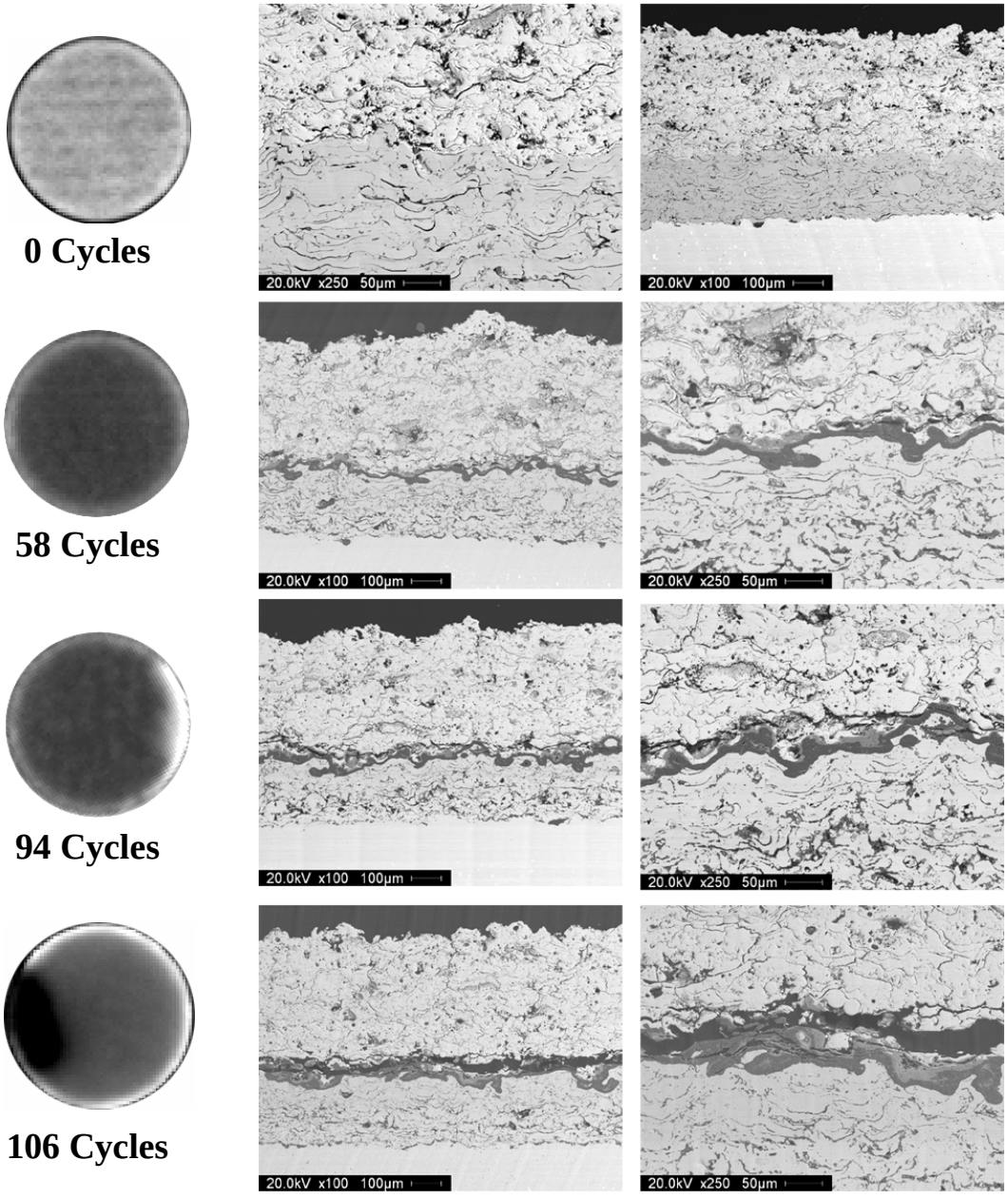

Figure 26. Thermal wave images and the corresponding cross-sectional backscatter electron micrographs of TBCs as a function of 10-hour thermal cycling at 1150°C.

For TBCs, thermal contact resistance between oxides (e.g., YSZ and TGO) and substrate (e.g., bond coat and superalloys) can vary in the presence of defects, cracks, and delaminations, at or near interfaces, giving rise to variation in heat transfer rate according to Eq. 8**.**[10,12] The heat transfer rate will locally change causing the surface temperature of the YSZ topcoat to remain higher on the damaged region. This is clearly shown in Figure 27 with a profile of the thermal wave amplitude and the corresponding cross-sectional micrograph of delaminated TBC specimen. The brighter region with a large amplitude (~700) of thermal wave response corresponds to a completely delaminated YSZ coating. The darker region with a small thermal wave amplitude (<400) corresponds to an in-tact YSZ coating as presented in detailed backscatter micrograph in Figure 28(a). The damage at a microstructural scale presented in Figure 28(b) corresponda to a thermal wave amplitude of approximately 500 as indicated by region “B” in Figure 27**.**

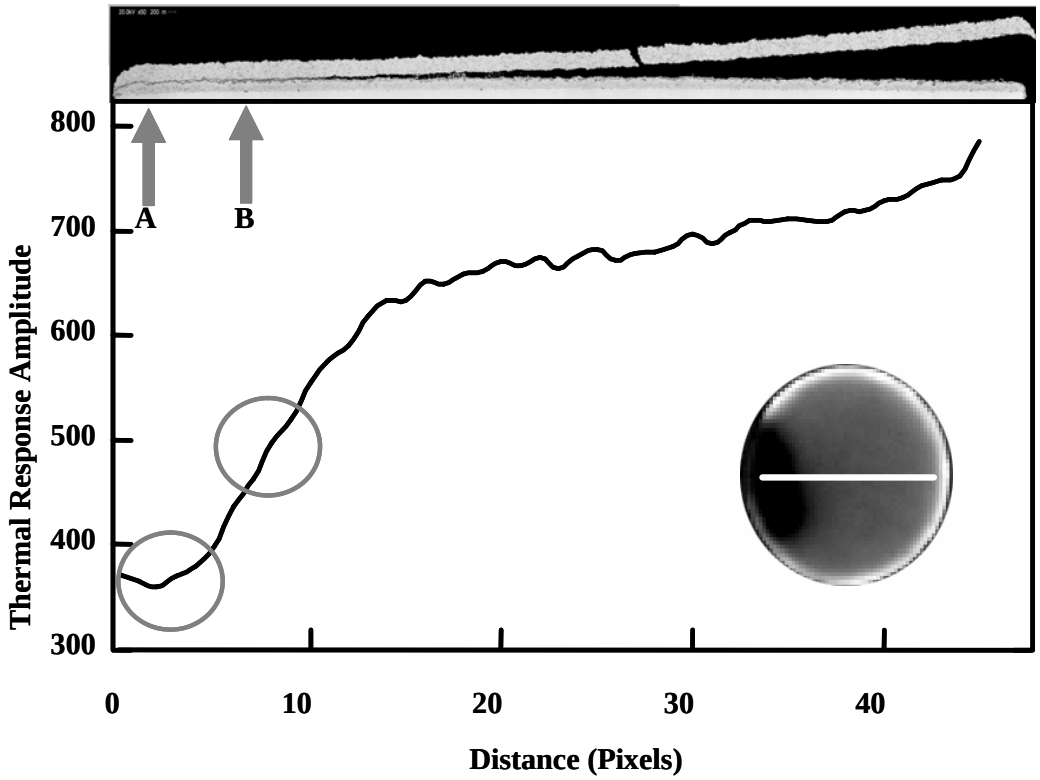

Figure 27. Cross-sectional micrograph, thermal wave image, and thermal wave response profile of a partially delaminated TBC specimen. The thermal response amplitude is low within the adhered region, and is high in the completely delaminated region

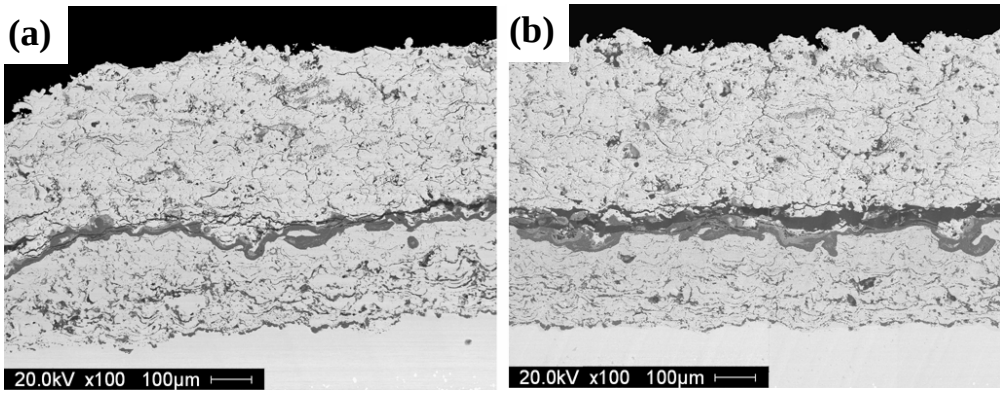

Figure 28. Detailed backscatter micrographs from specified areas in Figure 8: (a) in the intact region "A" with a low thermal amplitude of ~400 and (b) in the microstructurally damaged region "B" with an intermediate amplitude of ~500.

4.3.2. Electron Beam Physical Vapor Deposited Thermal Barrier Coatings

Figure 29 presents backscatter electron micrographs of the as-coated EB-PVD TBC. These TBCs exhibited a strain tolerant columnar microstructure and a thin TGO layer. Since there was no surface treatment (i.e. shot peening, grit blasting, etc.) prior to deposition of the ceramic topcoat, the morphology of the interface between the YSZ and bond coat was smooth except for ridges associated with the bond coat grain boundaries that results from CVD processing.

Backscatter electron micrographs corresponding to 10% of the average thermal cyclic lifetime are shown in Figure 30 and Figure 31. During thermal cycling, there was uniform growth of the TGO scale. A phase transformation in the bond coat was commonly associated with ridges. Initial damage was observed as shown in Figure 31(a) within the ceramic, (b) at the YSZ/TGO interface, and (c) within the TGO. Two regions were observed in the TGO: a mixed-oxide zone (MOZ) near the YSZ comprised of Al_2O_3 and YSZ; and a continuous layer of Al_2O_3 near the bond coat (continuous oxide zone (COZ)). The MOZ forms during deposition and typically consists of Zr and Y rich-particles dispersed in an Al_2O_3 matrix. The COZ is typically dense and consists of α-Al_2O_3. Cracks that formed within the TGO were between the MOZ and the COZ as shown at high magnification in Figure 32.

Figure 33 displays the backscatter images of the specimens after 70% thermal cyclic lifetime. These images, again, show a growth in TGO thickness and increased damage: within the ceramic, at the YSZ/TGO interface, within the TGO, and at the TGO/bond coat interface. Preferential oxidation and subsurface damage was prevalent at the grain boundary ridges.

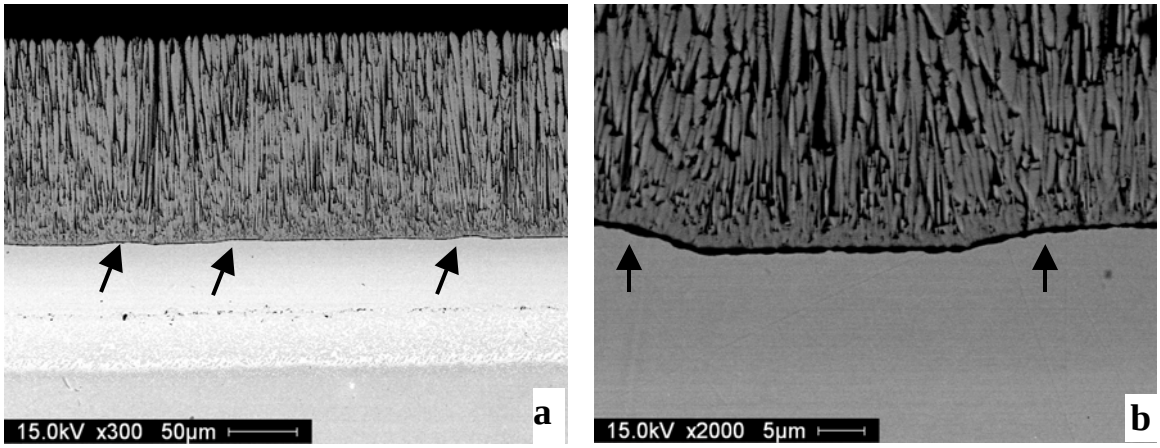

Figure 29. Typical backscatter electron micrographs of the EB-PVD specimens at (a) 300x and (b) 2000x. Ridges indicated by arrows were present as a result of processing.

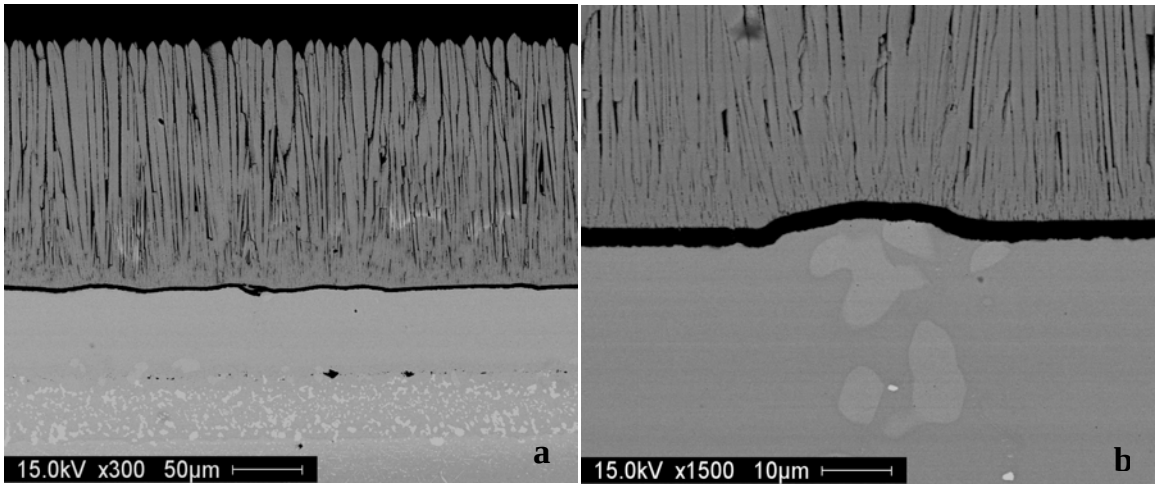

Figure 30 Typical backscatter electron micrographs of EB-PVD TBC specimens after 10% lifetime at (a) 300x and (b) 1500x.

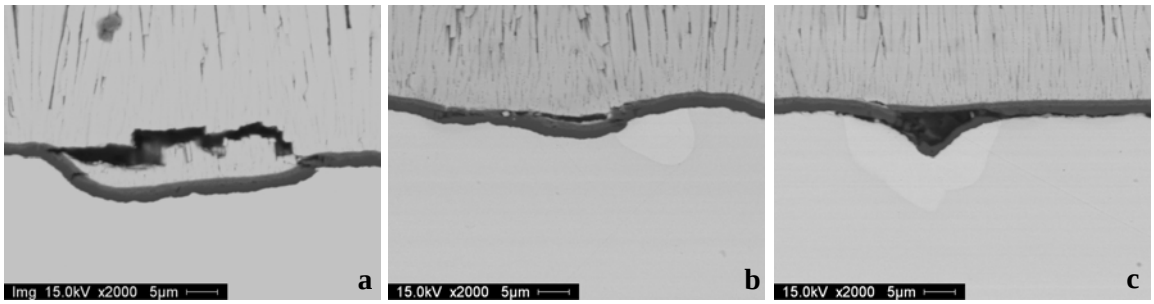

Figure 31. High magnification backscatter images after 10% lifetime displaying damage initiation (a) within the ceramic topcoat near the TGO, (b) within the YSZ/TGO interface, and (c) within the TGO.

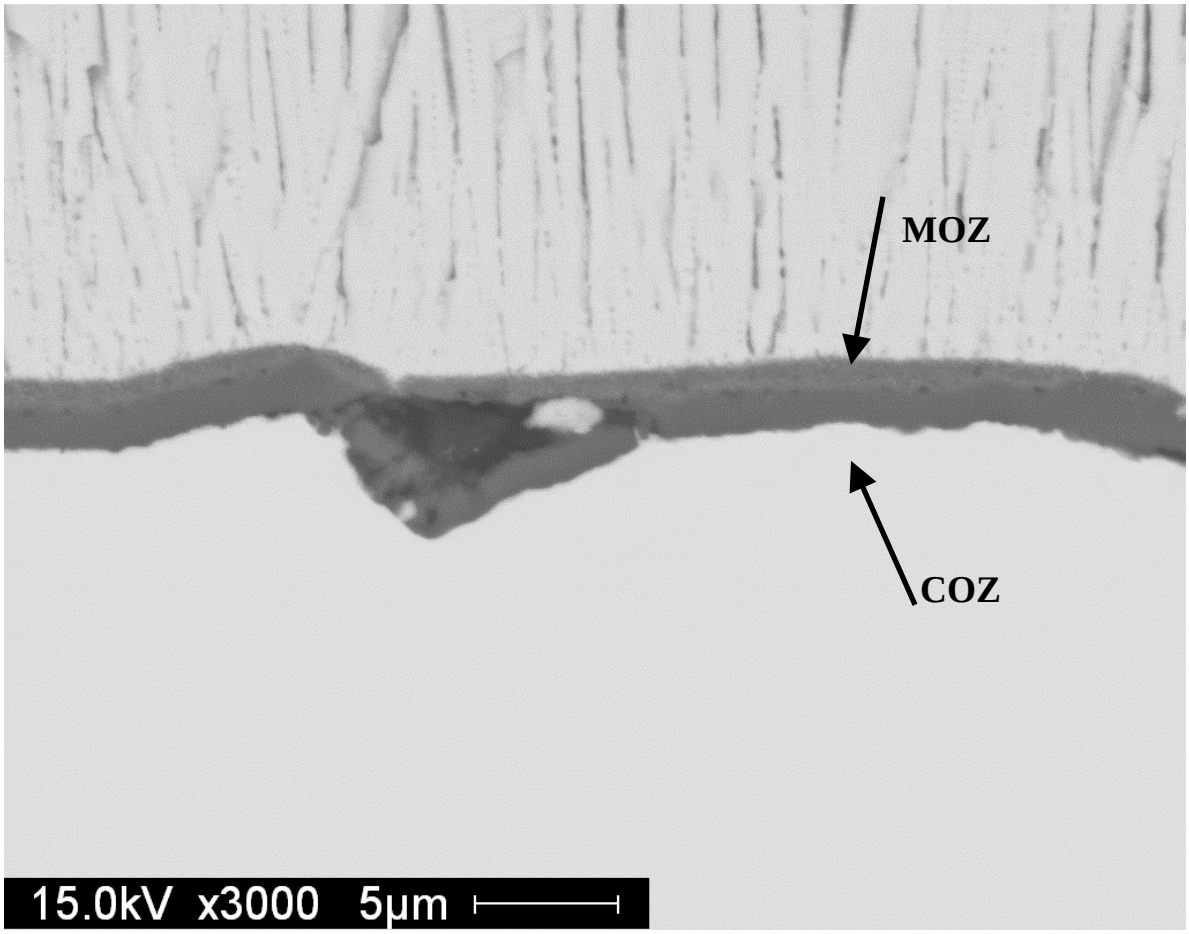

Figure 32. High magnification micrograph of initial damage within the TGO. Cracks formed between the MOZ and COZ.

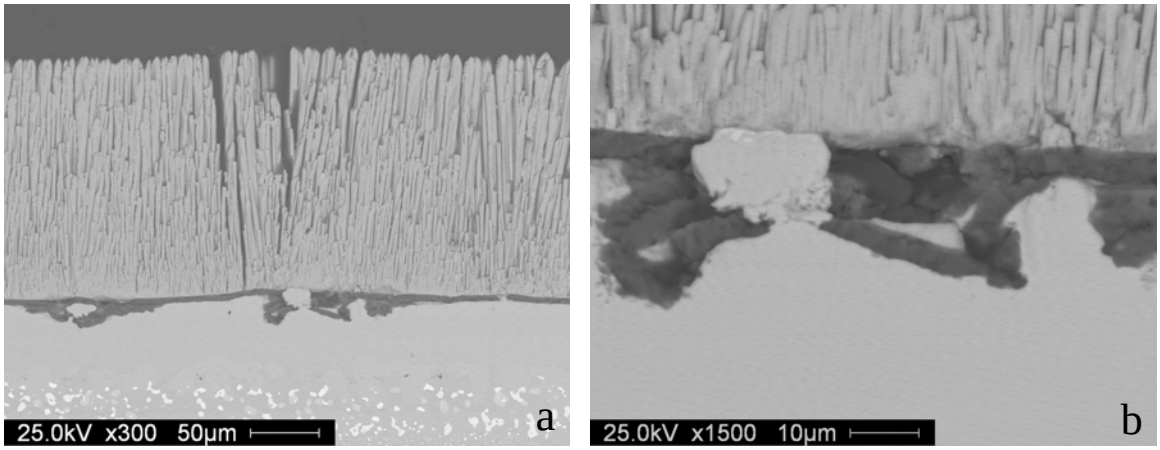

Figure 33. Typical backscatter electron micrographs of EB-PVD TBC specimens after 70% lifetime at (a) 300x and (b) 1500x.

The average lifetime of the specimens was 406 cycles ± 22 cycles. Typical spallation occurred by buckling as shown in the macro photographs in Figure 34. Backscatter electron micrographs of spallation surfaces of the specimens are represented in Figure 35. Microscopic constituents of YSZ and TGO were observed on both the bottom of the spalled-YSZ in Figure 35 (a) and (b) and on the bond coat surface where YSZ coating has spalled off in Figure 35 (c), (d), and (e). Presence of MOZ and metallic surface of (Ni,Pt)Al bond coats were also observed on the top surface of the bond coat. These micrographs indicate that the fracture for the spallation occurred within YSZ, at the interface between YSZ and TGO, and within the TGO between the MOZ and COZ. Most of the TGO observed on the fracture surface indicates the intimate relationship between grain boundary ridges of (Ni,Pt)Al bond coat.

After spallation, cross-sectional secondary electron micrographs demonstrated a preferential oxidation of the bond coat below the ridges associated with the grain boundaries as presented in Figure 36. However, it should be noted that the crack at the asperity tip of the grain boundary ridges are not necessarily observed with the preferential oxidation of grain boundaries.

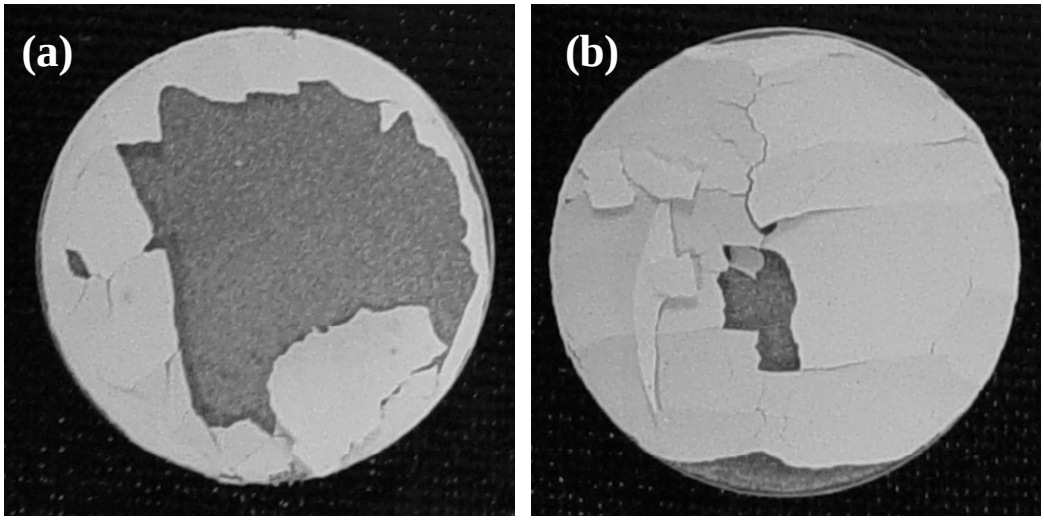

Figure 34. Macro photographs of spalled EB-PVD specimens show that buckling was the mode of failure.

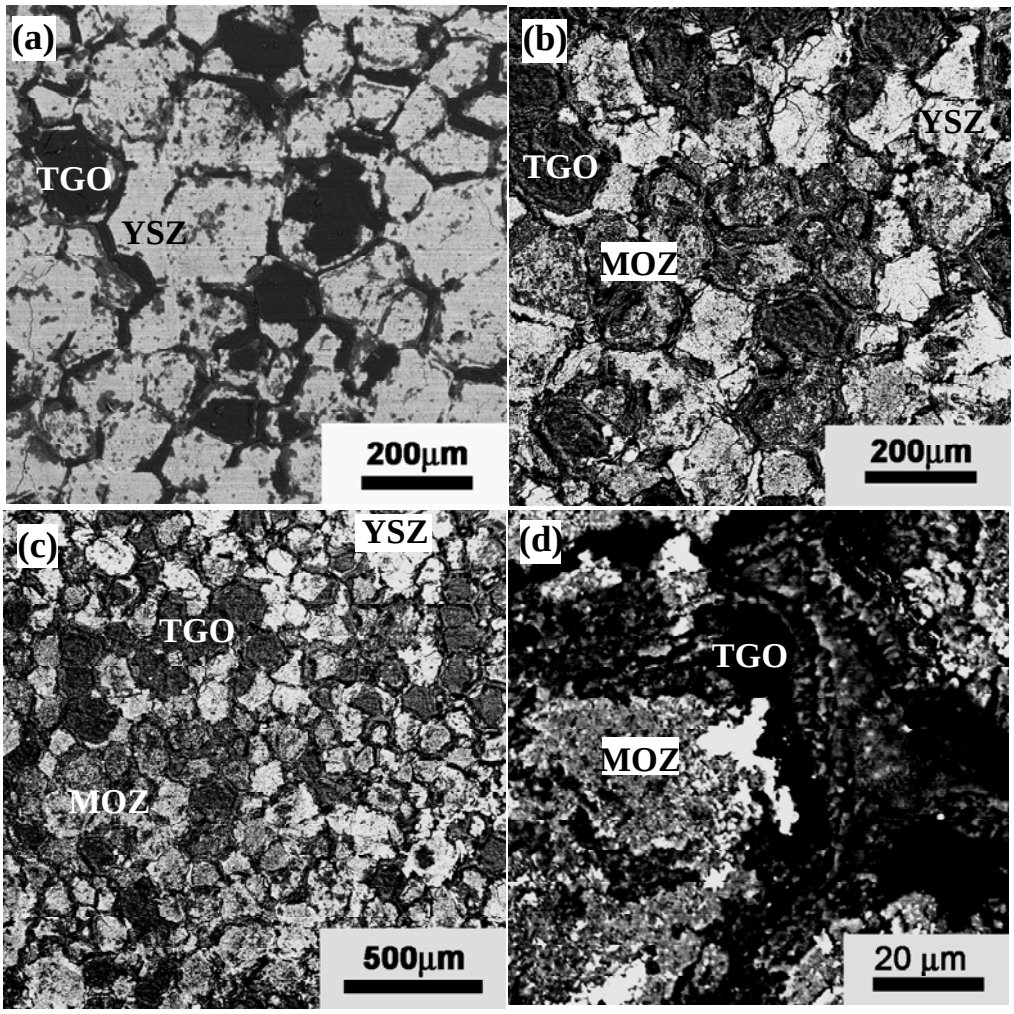

Figure 35. Backscatter electron micrographs of fracture surfaces in EB-PVD TBCs (a) on the bottom of the spalled-YSZ coating, and (b, c, and d) on the top of bond coat fracture surface.

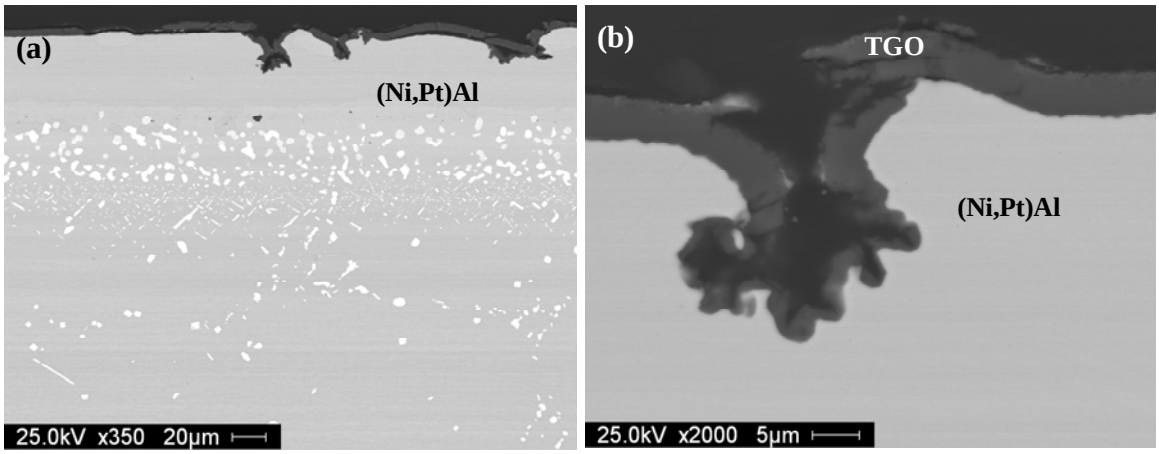

Figure 36. Cross-sectional backscatter electron micrographs TBCs after spallation of EB-PVD YSZ showing the preferential oxidation of (Ni,Pt)Al bond coat along the grain boundaries associated with ridges.

5. DISCUSSION

5.1. Applicability of Thermal Wave Imaging and Failure Mechanisms of Air Plasma Sprayed Thermal Barrier Coatings

The experimental amplitude of the thermal wave response as a function of time is plotted for TBCs with three different YSZ thicknesses in Figure 37. The thermal response amplitude calculated using Eq. 7 is also plotted in Figure 37 using material constants $\alpha = 5 \times 10^{-7}$ m^2/s, $\rho =$ 5 g/cm^3, and $c = 455$ J/kg-K, and $Q = 3125$ kJ. This value of Q was chosen to match the initial absolute thermal wave response measured from the TBC specimens. While a distinction in thermal wave amplitude does not occur initially (up to 0.33 seconds), variation in the amplitude as a function of YSZ thickness was observed after 0.4 seconds as presented in Figure 37, particularly for YSZ coatings with 380μm in thickness. Therefore an acquisition time to detect subcritical-subsurface damage for TBCs with YSZ thickness of 380μm was determined to be 0.37 seconds. Similar deviations in amplitude from Eq. 7 occur for the 635μm and 1015μm coatings. By having the ability to distinguish the time at which the thermal diffusion occurs through the YSZ/bond coat interface (e.g., deviation from Eq. 7), it is possible, with calibration, to non-destructively attain thickness measurements of the specific YSZ coatings.

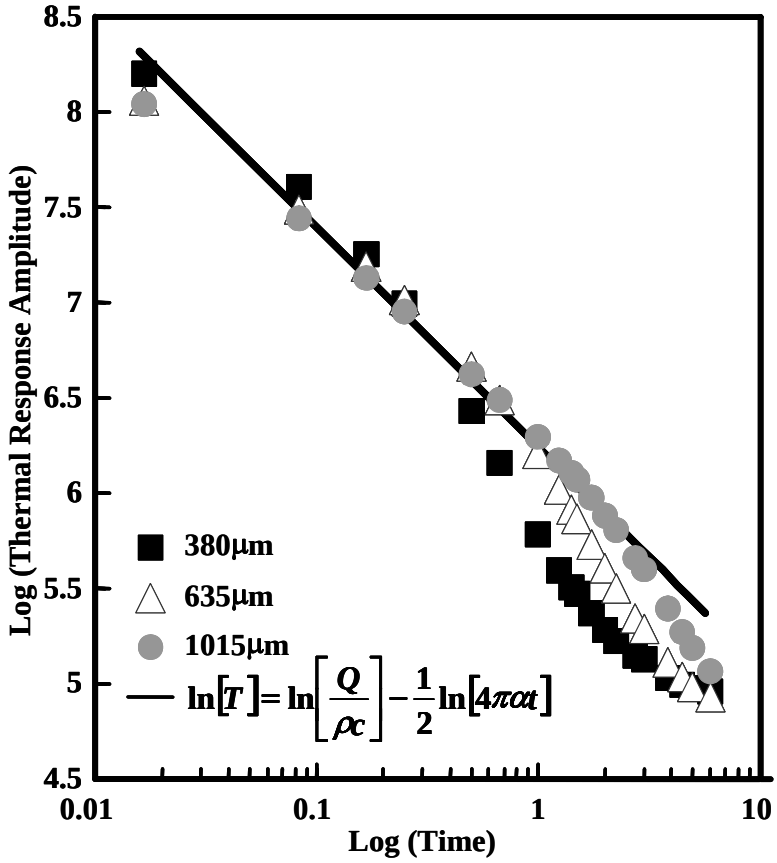

Figure 37. The average thermal wave amplitude from APS TBC specimens as a function of time following thermal flash heating is plotted with the 1-dimensional law of conduction in log form.

As displayed in Figure 37, the heat transfer through the YSZ followed a one-dimensional linear trend during the initial acquisition period (e.g., up to 0.4 second for 380μm-thick YSZ). Since the microstructure of as-coated YSZ contains pores and splat-quenched cracks particularly at splat boundaries, there may be an uncertainty to the assumption of linear heat diffusion since one-dimensional flow cannot be applied to a porous medium.[74] However, according to Figure 37, analysis based on one dimensional heat conduction may be sufficient during the initial acquisition periods, and indicates that the thermal diffusion must be much less in the lateral direction than that in the longitudinal direction.

The average thermal response amplitude plotted in Figure 20 initially shows a high amplitude in the as-received condition, greater than the average thermal response for highly damaged specimens. After 22 thermal cycles, the thermal response amplitude decreased. The cause for the decrease is not fully understood. It may, in part, be a result of the formation of the TGO, sintering, and variation in oxygen stoichiometry for as-coated YSZ. Radiation and absorption of the thermal response were not considered in this study. YSZ is non-absorbing over much of the specified infrared region (i.e. 6 – 9 μm) and the TGO may alter the absorbance and reflectance of heat displaying a dark contrast in thermal images once developed.

Final spallation of the APS TBCs with NiCoCrAlY bond coats was by flat failure in one large intact piece. In the as-received condition, the microstructure of the YSZ was porous with macro- and micro-cracks at splat boundaries due to processing. The bond coat also displayed splat boundaries from processing. The interface morphology between the ceramic topcoat and metallic bond coat was rough, yet did not display strong evidence of a sinusoidal pattern. No TGO was observed prior to thermal cycling.

After 58 thermal cycles, the TGO was well developed and sintering of the YSZ resulted in a less porous topcoat and closing of microcracks. A few mesocracks were observed in the ceramic near the TGO due to out-of-plane stresses arising in highly stressed regions of the TGO as well as due to topcoat sintering.[38,39,40]

By 94 thermal cycles, near the end-of-life for the specimens, mesocracks propagated and coalesced into larger cracks within the ceramic and partially within the TGO. This was influenced by the thickening of the TGO and the stress distribution within the ceramic and the TGO. Just prior to final spallation, the subsurface cracks coalesced into one large crack propagating across the specimen, observed in Figure 27, causing flat failure of the TBC.

Nucleation of mesocracks in the ceramic near the TGO is showing in Figure 26 after 58 cycles. According to Figure 20, the change in thermal response from 40 cycles and 58 cycles was quite similar, indicating that the mesocracks were not detected with TWI. Between 58 and 70 cycles, the change in thermal response displayed an increase in amplitude and it should be noted that one specimen failed at this cyclic lifetime. After 94 cycles, there was another increase in the change of thermal response that can be attributed to the formation of delaminations. After 94 thermal cycles, the microstructure displayed large cracks at the TGO/YSZ interface as presented in Figure 26. Since the average thermal response between 70 and 94 cycles is similar, and one specimen failed after 70 cycles, the rise in thermal response amplitude between 58 and 70 cycles may be due to the coalescence of mesocracks to form large detectable cracks.

TWI for APS TBCs is a quick, convenient technique that is non-intrusive, yet there are some limitations to this technique. TWI is beneficial as a surface evaluation technique. Deep defects buried beneath the surface have reduced resolution and accuracy of the flaw size in the thermal image. Typically, the size of the flaw is detectable if it is one to two times larger than its depth beneath the surface.[75] The large contrast in the thermal images from edge delaminations may be too late for damage detection, since spallation occurred soon after initiation. More investigation on the value of the thermal response amplitude associated with subsurface damage is needed for quantitative analysis.

5.2. Damage Detection with Photostimulated Luminescence Spectroscopy and Failure Mechanisms for Electron Beam Physical Vapor Deposited Thermal Barrier Coatings

The mechanism of final spallation of the EB-PVD TBCs with as-coated (Ni,Pt)Al bond coat was by buckling. Often, damage progression by microcrack extension and link-up leads to

large crack propagation subsequent to buckling. The appearance of ridges in the as-received condition served as bond coat defects or irregularities and may be associated with bond coat grain boundaries.

The thermal mismatch between the bond coat and oxide during cycling is the cause for fatigue. At peak temperature, the oxide grows at a relatively low stress on a soft bond coat with low residual stresses. During cooling, the thermal mismatch between the oxide and the substrate causes the metallic bond coat to contract faster inducing compressive stresses in the TGO.[69,57,76,77] In the presence of ridges, tensile stresses form in the TGO creating through thickness cracks that allow oxygen to penetrate the bond coat at grain boundaries and create a site for preferential oxidation of the bond coat. Initial damage is shown at high magnification in Figure 31 after ~10% lifetime (a) within the ceramic near the TGO, (b) at the TGO/YSZ interface, and (c) within the TGO (i.e. between the MOZ and COZ). Through thickness cracks are visible for the three types of initiation sites. Figure 31(b) and (c) show bond coat phase transformation from β to γ/γ' as a result of aluminum depletion near the through-thickness cracks creating accelerated oxidation of the bond coat.

As the number of cycles increased, the bond coat, upon cooling, contracted more than the oxide. The repeated compressive stresses in the TGO caused tensile plastic straining of the bond coat, which widened the cavities. With altered geometry from the progression of damage over thermal cycling, the fracture plane changed frequently between the bond coat/TGO interface, within the TGO, and at the YSZ/TGO interface.[78] The link-up of microcracks created a single large crack beneath the TBC surface which led to rapid crack link-up and macro-crack propagation, causing the subsurface defect to become a critical size for buckling spallation.

Damage was observed initially after 10% lifetime within the YSZ, at the YSZ/TGO interface, and within the TGO in the vicinity of bond coat ridges. The damaged areas were quite small in comparison with the probe size and luminescence was detected from compressive residual stress in the TGO.

With continued thermal cycling, ratcheting of the bond coat caused cavities to form near bond coat grain boundary ridges. Damage beneath the EB-PVD TBC surface was detected with PL after ~50% lifetime. Closer to the end-of-life, heavy damage was observed in all facets: within the YSZ, between the YSZ/TGO interface, and within the TGO.

In areas where TGO was cracked (i.e., between COZ and MOZ), the portion of TGO adhering to the YSZ was not affected by compressive stress inflicted by thermal expansion mismatch upon cooling. A rise in luminescence near the R-line frequencies for α-Al_2O_3 (i.e. ν = 14402cm^{-1} and ν = 14432cm^{-1}) indicated that some of the TGO was relieved of the compressive residual stress. Stress-relief was a result of damage accumulation within the TGO over cyclic oxidation.

The evolution of luminescence due to stress-relief developed after ~50% lifetime and displayed an increase of both relative intensity and population. The relative intensity of the luminescence associated with stress-relief was initially relatively weak, and increased in intensity with thermal cycling. The low intensity may result from small amounts of damage as compared to the PL probe detection area. The probe area is relatively large, displaying signal mostly from intact TGO under compressive residual stress. The relative intensity increased due to either an increase in damaged area and/or increase in occurrences. Of the 20 random spot measurements, the population of spectra which exhibited luminescence from stress-relief increased with thermal cycling until spallation occurred.

The compressive residual stress determined from PL for the EB-PVD TBCs with (Ni,Pt)Al bond coats had high amplitude (e.g. 8GPa) in comparison to reported values in literature. The cause for such high stress is not certain. The bond coat was processed without any surface treatment prior to YSZ deposition (i.e. shot-peening, grit-blasting, etc.) This investigation was part of a larger study that involved a variety of TBC specimens from five industrial partners. One batch of specimens comprised of an EB-PVD YSZ with a grit-blasted (Ni,Pt)Al bond coat. PL was collected for both samples consecutively throughout the experiment. Figure 38 is a comparison between luminescence spectra from the specimens under investigation shown in black and specimens with grit-blasted bond coat in grey. Comparison of spectra from the current specimen and the grit blasted specimen indicates two points: high stresses were not a result of machine error and the high stresses may be a result of bond coat processing.

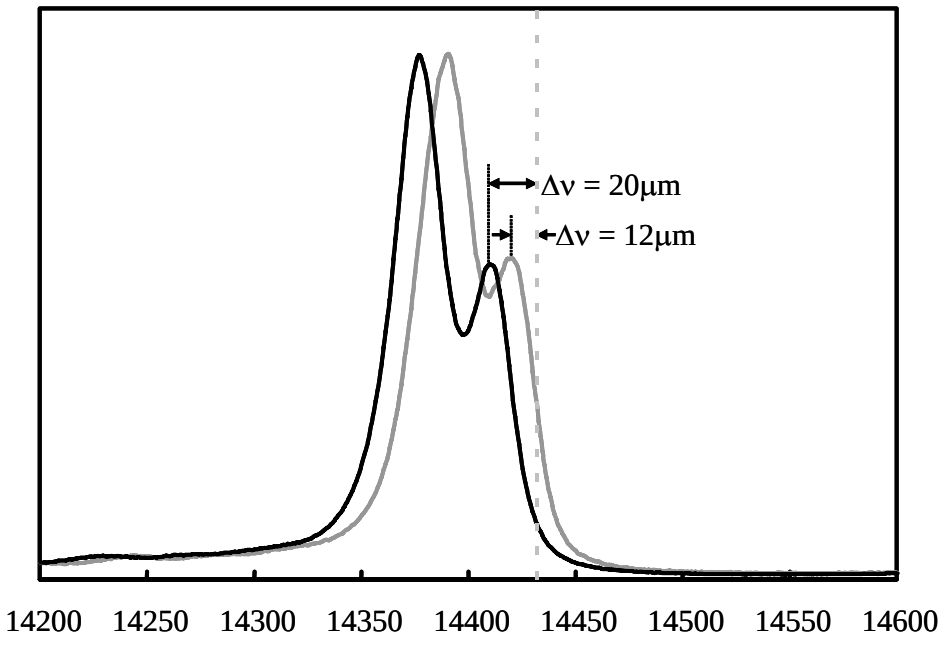

Figure 38. Typical spectrum from this study is shown in black. It is compared with a spectrum from another study in which PL was collected simultaneously. The specimens from the second study had an EB-PVD topcoat with a grit-blasted (Ni,Pt)Al bond coat (grey).

6. SUMMARY

The present study aimed to investigate the applicability of two NDE techniques for health monitoring, damage detection, and/or quality control of TBCs. APS TBCs were evaluated with TWI. The thermal responses from TBCs of varying thicknesses were analyzed using the 1-D law of conduction. It was found that heat dissipation through the TBC following pulsed excitation by xenon flash lamps initially followed the 1-D law of conduction and deviated from it as a function of thickness and time. The deviation resulted from quick dissipation of heat into the conductive metallic substrate. Therefore, with calibration, TWI can be used as a tool for YSZ thickness measurements of APS TBCs in the as-coated condition for quality control measures.

APS TBCs with 380 μm YSZ were evaluated with TWI as a function of thermal cycling. Near the end-of-life, bright regions in the thermal image indicated delaminations prior to spallation. The health of the TBC was monitored by a rise in thermal response amplitude which may indicate a coalescence of microcracks to a detectable level.

PL detected stress-relief in the TGO scale of EB-PVD TBCs with (Ni,Pt)Al bond coat. PL near the R-line frequency for polycrystalline α-Al_2O_3 without any residual stress (i.e. ν = 14402cm^{-1} and ν = 14432cm^{-1}) began to appear after ~50% average lifetime of the specimens. The rise in luminescence corresponded to a damage within the TGO between the MOZ and COZ. In regions of cracked TGO, the MOZ adhering to the YSZ was not exposed to compressive stresses from thermal expansion mismatch upon cooling.

Metastable phases were detected with PL using to defined curve-fitting parameters. The polymorphic transformation from a metastable phase to equilibrium α-Al_2O_3 was also detected. Since metastable phases are thought to be detrimental to coating lifetime, detection of these phases by PL can be a quality control tool.

7. APPENDIX A: PUBLICATIONS AND PRESENTATIONS

Publications

- B. Jayaraj, **B. Franke**, D. Miranda, S. Laxman, J.W. Byeon, Y. H. Sohn, "Evolution of Photostimulated Luminescence during Thermal Cycling of Electron Beam Physical Vapor deposited Thermal Barrier Coatings," ASME- GT2005-69121, in press.
- **B. Franke**, Y.H. Sohn, X. Chen, J.R. Price, "Monitoring Damage Evolution in Thermal Barrier Coatings with Thermal Wave Imaging," Surface and Coatings Technology, in press
- B. Jayaraj, **B. Franke**, J.W. Byeon, Y.H. Sohn, "Life Time Comparison of Thermal Barrier Coatings with Air Plasma Sprayed/ Vacuum Plasma Sprayed NiCoCrAlY Bondcoat," Metallurgical and Materials Transactions A, in preparation
- **B. Franke**, Y.H. Sohn, X. Chen, J.R. Price, Z. Mutasim, "Thermal Wave Imaging Application in Thermal Barrier Coatings," Proceedings on the 29th International Conference on Advanced Ceramics and Composites- CB-S2-42-2005, in press
- Y.H. Sohn, B. Jayaraj, S. Laxman, **B. Franke**, J.W. Byeon, A.M. Karlsson, "The Non-Destructive and Nano-Microstructural Characterization of Thermal-Barrier Coatings," Journal of Metals, pp 53-56, October 2004
- S. Laxman, **B. Franke**, B.W. Kempshall, Y.H. Sohn, L.A. Giannuzzi, K.S. Murphy, "Phase Transformation of Thermally Grown Oxide on (Ni,Pt)Al Bond Coat During Electron Beam Physical Vapor Deposition and Subsequent Oxidation," *Surface and Coatings Technology* 177-178 (2004) 121-130

Presentations

- **B. Franke**, Y.H. Sohn, X. Chen, J.R. Price, "Monitoring Damage Evolution in Thermal Barrier Coatings with Thermal Wave Imaging," 2005 International Conference on Metallurgical Coatings and Thin Films – ICMCTF, May 2 – May 6, 2005, San Diego, CA, USA
- **B. Franke**, Y.H. Sohn, X. Chen, J.R. Price, Z. Mutasim, "Thermal Wave Imaging Application in Thermal Barrier Coatings," 29th International Conference on Advanced Ceramics and Composites, January 25, 2005, Cocoa Beach, FL, USA
- **B. Franke**, B. Jayaraj, "Non-destructive Evaluation of Thermal Barrier Coatings by Photostimulated Luminescence Spectroscopy with Respect to Thermal Cycling," 2004 International Surface Engineering Congress and Exhibition, August 2 – August 4, 2004, Orlando, FL, USA
- **B. Franke**, B. Jayaraj, "Non-destructive Evaluation of Thermal Barrier Coatings by Photostimulated Luminescence Spectroscopy with Respect to Thermal Cycling," Showcase of Undergraduate Research Excellence, University of Central Florida, April 9, 2004

8. REFERENCES

[1] J. C. Zhao and J. H Westbrook, *MRS Bulletin*, 28 (9) (2003) 622

[2] M. Donachie, Jr., "Superalloys," Materials Park, OH 1984

[3] R. Bowman, As a supplement to The Minerals, Metals & Materials Society's website dedicated to the 9th International Symposium on Superalloys <http://www.tms.org/Meetings/Specialty/Superalloys2000/SuperalloysHistory.html>

[4] R.L Jones "Metallurgical and Protective Coatings," K.H. Stern, ed. Chapman and Hall, London, 1996, p197

[5] P.K. Wright and A.G. Evans, *Current Opinion in Solid State Materials Science*, 4 (1999) 255

[6] R.A. Miller, *Surface and Coatings Technology*, 30 (1987) 1-11

[7] N.P. Padture, M. Gell, and E.H. Jordan, *Science*, 296 (2002) 280

[8] A.G. Evans, D.R. Mumm, J.W. Hutchinson, G.H. Meier, and F.S. Pettit, *Progress in Material Science* 46 (2001) 505

[9] J.M. Milne, W.N. Reynolds, *SPIE Proceedings*, 520 (1984) 119

[10] G. Newaz and X. Chen, *Surface and Coatings Technology*, 190 (2005) 7

[11] Z.A. Chaudhury, G.M. Newaz, S.Q. Nusier, and T. Ahmed, *Mateials Science and Engineering*, A231 (1997) 34

[12] X. Chen, Progressive Damage and Failure of Thermal Barrier Coatings, Ph.D. Dissertation, Wayne State University, Detroit, 2001

[13] Y. Tamarin, "Protective Coatings for Turbine Blades," Materials Park, OH 2002 p161-162

[14] M. Chen, B. Hallstedt, and L.J. Gauckler, *Solid State Ionics*, 170 (2004) 255

[15] P.V. Ananthapadmanabhan, "Non-equilibrium Processing of Materials" C. Suryanarayana, ed. Pergamon, New York, 1999 p130

[16] T.A. Dobbins, R. Knight, and M.J. Mayo, *Journal of Thermal Spray Technology*, 12 (2) (2003) 214-225

[17] ASM Metals Handbook Desk Edition Online: Metals Handbook Desk Addition, ASM International , Materials Park, OH, 2001 <http://products.asminternational.org/asm/servlet/Navigate>

[18] D.R. Clarke and C.G. Levi, *Annual Review of Materials Science*, 33 (2003) 383

[19] G.H. Meier and F.S. Pettit, *Materials Science and Engineering* A153 (1992) 548

[20] D.L. Ruckle and D.S. Duvall, US Patent 445794, 3 Aug. 1984

[21] T.E. Strangman, U.S. Patent 4321311, 23 March 1982

[22] S.R. Choi, D. Zhu, and R.A.Miller, *NASA*/TM-2004-212625

[23] E.A.G. Shillington and D.R. Clarke, *Acta Materialia*, 47 (4) (1999) 1297

[24] V.K. Tolpygo and D.R. Clarke, *Acta Materialia*, 48 (13) (2000) 3283

[25] V.K. Tolpygo and D.R. Clarke, *Acta Materialia*, 52 (2004) 5115

[26] S. Laxman, B. Franke, B.W. Kempshall, Y.H. Sohn, L.A. Giannuzzi, and K.S. Murphy, *Surface and Coatings Technology*,

[27] K.S. Murphy, K.L. More and M.J. Lance, *Surface and Coatings Technology* 147-147 2001 152

[28] M.W. Brumm and H.J. Grabke, *Corrosion Science*, 33 (11) (1992) 1677

[29] S. Laxman, Unpublished Research

[30] V.K. Tolpygo and D.R. Clarke, *Materials at High Temperatures*, 17 (2000) 59

[31] J.S. Wang and A.G. Evans, *Acta Materialia* 46 (14) (1998) 4993

[32] J. S. Wang and A.G. Evans, *Acta Materialia* 47 (2) (1999) 669

[33] J. Liu, Y.H. Sohn, *Surface and Coatings Technology*, in press

[34] V.K. Tolpygo, *Surface and Coatings Technology*, in press

[35] X. Peng, D.R. Clarke, *Journal of the American Ceramic Society*, 83 (5) (2000) 1165

[36] Y. H. Sohn, B. Jayaraj, S. Laxman, B. Franke, J. Byeon, and A.M. Karlsson, *Journal of Metals*, 56 (10) (2004) 53

[37] D.R. Clarke and W. Pompe, *Acta Materialia*, 47 (6) (1999) 1749

[38] E. P. Busso, J. Lin, and S. Sakurai, *Acta Materialia*, 49 (2001) 1529

[39] A. M. Freborg, B.L. Ferguson, W.J. Brindley, G.J. Petrus, *Materials Science and Engineering*, A245 (1998) 182

[40] A. G. Evans, G.B. Crumley, and R.E. Demaray, *Oxidation of Metals*, 20 (1983) 193

[41] A. Rabiei and A.G. Evans, *Acta Materialia* 48 (2000) 3963

[42] K.W. Schlichting, N.P. Padture, E.H. Jordan, and M. Gell, *Materials Science and Engineering*, A342 (2003) 120

[43] E. P. Busso, J. Lin, S. Sakurai, and M. Nakayama, *Acta Materialia*, 49 (2001) 1515

[44] Y.H. Sohn, J.H. Kim, E.H. Jordan, and M. Gell, *Surface and Coatings Technology* 146-147 (2001) 70-78

[45] M. Gell, K. Vaidyanathan, B. Barber, J. Cheng, and E.H. Jordan, *Metallurgical and Materials Transactions*, 30A (1999) 427

[46] A.V. Luikov, "Analytical Heat Diffusion Theory," Academic Press, NY, pp381, 1968

[47] X. Chen, G. Newaz, and X. Han, Proceedings of 2001 ASME International Mechanical Engineering Congress and Exposition IMECE2001/AD-25323

[48] P.G. Bison, S. Marinetti, E. Grinzato, V.Vavilov, F.Cernucchi, and D. Robba, *Proceedings of SPIE: Thermosense XXV*, 5073 (2003) 318

[49] B. Franke, Y.H. Sohn, X. Chen, J. Price, and Z. Mutasim, *Proceedings of the 29th International Conference and Exposition on Advanced Ceramics and Composites*, Jan. 23-28, 2005, FL, in Press.

[50] P.G. Klemens and M. Gell, *Mateials Science and Engineering*, A245 (1998) 143

[51] R. Siegel and C.M. Spuckler, *Mateials Science and Engineering*, A245 (1998) 150

[52] L. Grabner, *Journal of Applied Physics* 49 (2) (580) 1978

[53] D.M. Lipkin and D.R. Clarke, *Journal of Applied Physics*, 77 (5) (1995) 1855

[54] R.J. Christensen, D.M. Lipkin, D.R. Clarke, and K.S. Murphy, *Applied Physics Letters*, 69 (24) (1996) 3754

[55] D.M. Lipkin, D.R. Clarke, M. Hollatz, M. Bobeth, and W. Pompe, *Corrosion Science*, 39 (2) (1997) 231

[56] D.R. Clarke, R.J. Christensen, and V.K. Tolpygo, *Surface and Coatings Technology*, 94-95 (1997) 89

[57] V. Sergo and D.R. Clarke, *Journal of the American Ceramic Society*, 81 (1998) 3237

[58] K.W. Schlichting, K. Vaidyanathan, Y.H. Sohn, E.H. Jordan, M. Gell, and N.P. Padture, *Materials Science and Engineering*, A291 (1-2) (2000) 68

[59] M. Gell, E.H. Jordan, K. Vaidyanathan, K. McCarron, B. Barber, Y.H. Sohn, and V.K. Tolpygo, *Surface and Coatings Technology*, 120-121 (1999) 53

[60] Y.H. Sohn, K. Vaidyanathan, M. Ronski, E.H. Jordan, and M. Gell, *Surface and Coatings Technology*, 146-147 (2001) 102

[61] S. Sridharan, L. Xie, E.H. Jordan, and M. Gell, *Surface and Coatings Technology*, 179 (2-3) (2004) 286

[62] L.D. Xie, Y.H. Sohn, E.H. Jordan, and M. Gell, *Surface and Coatings Technology*, 176 (1) (2003) 57

[63] Y.H. Sohn, K. Schlichting, K. Vaidyanathan, E.H. Jordan, M. Gell, *Metallurgical and Materials Transactions*, 31A (2000) 2388

[64] K. Nakmoto, "Infrared and Raman Spectra of Inorganic and Coordination Compounds" 4th ed. John Wiley & Sons, NY 1986 p3-5

[65] Q. Ma and D.R. Clarke, *Journal of the American Ceramic Society*, 76 (1993) 1433

[66] Q. Ma and D.R. Clarke, *Journal of the American Ceramic Society*, 77 (1994) 298

[67] A.L. Schawlow, D.L. Wood, and A.M. Clogston, *Physics Review Letters*, 3 (1959) 271

[68] Q. Wen, D.M. Lipkin, and D.R. Clarke, *Journal of the American Ceramic Society*, 81 (1998) 3345.

[69] D.M. Lipkin and D.R. Clarke, *Oxidation of Metals*, 45 (1996) 267

[70] R.G. Munro, G.J. Piermarinin, S. Block, and W.B. Holzapfel, *Journal of Applied Physics*, 57 (2) (1985) 165

[71] J.A. Nychka and D.R. Clarke, *Surface and Coatings Technology*, 146-147 (2001) 110

[72] J. He and D.R. Clarke, *Journal of the American Ceramic Society*, 78 (5) (1995) 1347

[73] V.K. Tolpygo, J.R. Dryden, and D.R. Clarke, *Acta Materialia* 46 (1998) 927

[74] R. S. Shepard, J. Lhota, B. A. Rubadeux, D. Wang, and T. Ahmed, *Optical Engineering*, 42 (2003) 1337

[75] X. P. V. Maldague, "Theory and Practice of Infrared Technology for Non-destructive Testing," John Wiley & Sons, Inc, 2001

[76] V.K. Tolpygo and D.R. Clarke, *Oxidation of Metals*, 49 (1998) 187

[77] R. J. Christensen, V.K. Tolpygo, and D.R.Clarke, *Acta Materialia*, 45 (1997) 1761

[78] K. Vaidyanathan, M. Gell, and E.H. Jordan, *Surface and Coatings Technology*, 133-134 (2000) 28